Measurement and Identification of the Nonlinear Dynamics of a Jointed Structure Using Full-Field Data; Part I - Measurement of Nonlinear Dynamics

Wei Chen[a,b], Debasish Jana[c], Aryan Singh[d], Mengshi Jin[a,b], Mattia Cenedese[e], Giancarlo Kosova[f,g], Matthew R. W. Brake[h], Christoph W. Schwingshackl[i], Satish Nagarajaiah[c,h], Keegan J. Moore[d], Jean-Philippe Noël[j]

[a] *AECC Shanghai Commercial Aircraft Engine Manufacturing Co. LTD., Shanghai, 201306, China*

[b] *School of Aerospace Engineering and Applied Mechanics, Tongji University, Shanghai, 200092, China*

[c] *Civil and Environmental Engineering, Rice University, Houston, TX 77005, USA*

[d] *Department of Mechanical and Materials Engineering, University of Nebraska-Lincoln, Lincoln, NE 68588, USA*

[e] *Institute for Mechanical Systems, ETH Zürich, Leonhardstrasse 21, 8092 Zürich, Switzerland*

[f] *Siemens Industry Software, Leuven, Belgium*

[g] *Aerospace and Mechanical Engineering Department, University of Liège, Liège, Belgium*

[h] *Department of Mechanical Engineering, Rice University, Houston, TX 77005, USA*

[i] *Imperial College London, Mechanical Engineering, Exhibition Road, SW7 2AZ London, UK*

[j] *Control Systems Technology Group, Department of Mechanical Engineering, Eindhoven University of Technology, NL*

Abstract

Jointed structures are ubiquitous constituents of engineering systems; however, their dynamic properties (e.g., natural frequencies and damping ratios) are challenging to identify correctly due to the complex, nonlinear nature of interfaces. This research seeks to extend the efficacy of traditional experimental methods for linear system identification (such as impact testing, shaker ringdown testing, random excitation, and force or amplitude-control stepped sine testing) on nonlinear jointed systems, e.g., half Brake-Reuß beam, by augmenting them with full-field data collected by high-speed videography. The full-field response is acquired using high-speed cameras combined with Digital Image Correlation (DIC), which enables studying the spatial-temporal dynamic characteristics of the system. As this is a video-based experiment, additional constraints are attached to the beam at the node points to remove the rigid body motion, which ensures that the beam is in the view of the camera during the entire test. The use of a video-based method introduces new sources of experimental error, such as noise from the high-speed camera's fan and electrical noise, and so the measurement accuracy of DIC is validated using accelerometer data. After validating the DIC data, the measurements are recorded for several types of excitation, including hammer testing, shaker ringdown testing, fixed sine testing, and stepped sine testing. Using the DIC data to augment standard nonlinear system identification techniques, modal coupling and the mode shapes' evolution are investigated. The suitability of videography methods for nonlinear system identification of nonlinear beams is explored for the first time in this paper, and recommendations for techniques to facilitate this process are made. This article focuses on developing an accurate

data collection methodology as well as recommendations for nonlinear testing with DIC, which paves the way for video-based investigation of nonlinear system identification. In Part-II [1] of this work, the same data set is used for a rigorous assessment of nonlinear system identification with full-field DIC data.

Keywords: Jointed Structures, Nonlinear System Identification, Nonlinear System Testing, Digital Image Correlation (DIC), Full-field Measurements, Modal Interactions.

1. Introduction

Jointed structures are one of the most prevalent and vital constituents of numerous small to large scale engineering constructs [2]. Besides their primary task of providing structural stiffness and alignment to the structure, they are also known to be a source of nonlinearity, especially in energy dissipation [3, 4], which influences the dynamic response of the assembly. Accurate characterization and quantification of the nonlinear properties from the experiment are of great importance for understanding the dynamic behavior of a jointed structure. There are many nonlinear system identification techniques [5, 6, 7, 8, 9], which have been developed to construct a mathematical representation of the system of interest (usually in terms of amplitude-dependent natural frequencies and damping ratios or a polynomial describing the system's behavior). Due to the complexity of nonlinear dynamic behaviors (e.g., amplitude-dependent properties, jumps, sub/super harmonics, and modal interactions), nonlinear dynamic testing demands more data and effort than linear testing. The nonlinear dynamic test methods for mechanical systems can be categorized as free vibration response testing and forced vibration response testing based on external forces.

The commonly used free-response testing includes hammer testing and shaker ringdown testing. Hammer testing is a convenient method to obtain the frequency and damping properties for both linear and nonlinear systems [10]. For a nonlinear system, the system properties depend on the response amplitude, which necessitates that careful attention to the excitation levels be paid. Even though the hammer testing is convenient to conduct without introducing additional mass and stiffness, it excites the system with a broadband force, which results in most of the energy not being transmitted to the mode of interest. Consequently, data extracted from impact hammer testing spans a relatively small range of modal amplitudes, and often the nonlinearities of interest are not fully engaged. Another way to obtain the free response is shaker ringdown testing [11], or resonance decay testing [12], in which the system is excited by a sinusoid (or sinusoids) to steady-state with a high response amplitude, then the force from the shaker is withdrawn. In this manner, the identified instantaneous frequency, damping, and amplitude are from a single-mode response. The benefit of this method, compared to hammer testing, is that it can excite a specific mode to a high response level, and the responses are commonly dominated by this single mode. However, for operating this test, the sudden removal of the excitation usually leads to an impulsive loading on the structure, which may introduce the responses of the other modes. Moreover, for extracting the instantaneous damping for mechanical joints, the measured damping will be considerably affected if the shaker is attached to the structure due to an additional damping effect from the shaker [13].

The forced response testing includes stepped sine testing, phase resonance testing, and broadband excitation testing. At a constant output response amplitude level, mildly nonlinear systems are approximated as linear systems, and the obtained frequency response function (FRF) from

stepped sine testing is used to calculate the frequency and damping ratio, namely a single point in the backbone curve and damping-amplitude curve, respectively. Thus, amplitude-control stepped sine testing [14] (or force-control stepped sine testing [15]) is a relatively reliable method to characterize the nonlinear behavior based on FRFs. However, one disadvantage of this method is its low efficiency since one sweep only obtains one point in the backbone curve and damping-amplitude curve. Phase resonance testing (or force appropriation testing) [16], which tunes multiple shakers to excite a single-mode according to the phase lag quadrature criterion, has been widely used for large airplanes [17]. Based on the solid framework offered by the theory of Nonlinear Normal Modes (NNMs) [18], the phase resonance testing is extended to nonlinear systems [12] using multi-harmonic excitation to isolate an individual NNM. However, this method may consume a considerable amount of time in configuring the excitation forces. Control-based methods, such as the control-based continuation scheme [19] and phase-locked loop [20, 21], are potentially more robust to changes of stability and bifurcations. Compared to phase resonance testing, the phase-locked loop method is shown to be highly efficient in adjusting the excitations. Additionally, through proper feedback, the input force tends to be purely harmonic excitation by suppressing the super harmonics caused by the interaction between the specimen and the excitation system. However, since the state feedback is introduced, the effect of the control on the characteristics of the original system is difficult to evaluate. Nonlinear subspace identification methods [22, 23, 24], which are commonly implemented with broadband excitation testing, aim to construct a nonlinear state-space model to reproduce the dynamic responses of the test system. The advantages of this method are its ability to deal with multiple inputs and outputs data and to describe nonlinear behaviors without linearization. The deficiencies include its inapplicability to hysteretic nonlinearities and determination of the excitation levels of broadband excitation [25].

Accelerometers are the typical response acquisition approach used in the aforementioned test methods. Thus, most research extracts nonlinear behaviors through a limited number of distinct points on the structure. As such, these methods often do not capture the influence of the nonlinearity on the deflection shapes of the structure and, consequently, the information provided to existing nonlinear identification techniques is limited. The spatio-temporal distribution of the nonlinear properties has seldom been experimentally investigated. Recent advances in image-based measurement techniques, together with improvements in high-speed cameras, shed light on the appropriateness and accuracy of videography-based methods for measuring the response (both of discrete points and of the full-field) of a linear structure compared to more traditional approaches such as accelerometers and lasers [26, 27]. Significant advantages of videography include its low cost (at least compared to scanning Laser Doppler Vibrometers (LDVs)), non-contact, ease of operation, and multi-point vibration measurement from a pair of cameras [28]. The state-of-the-art vision-based techniques can be categorized as the target-less method [29, 30], the point tracking (PT) [31], and digital image correlation (DIC) [32, 33, 34], which are widely reported in review papers [35, 36, 37, 38]. The target-less method, which is based on computer vision extraction, does not require any surface preparation work, and is commonly used in structural health monitoring of civil engineering structures [39]. Both the PT method and DIC require surface preparation and, therefore, provide higher quality measurements [35]. In particular, DIC is a class of non-contact methods that acquires images of an object and performs image analysis to extract the full-field shape, deformation, and motion of the object [40, 41]. Compared with the PT method, which tracks the motion of a single or discrete set of points, DIC can extract full-field responses [42], and is advantageous when high spatial density is required [43]. In the context of structural dynamics,

DIC has already been used to study the slip and separation of jointed interfaces [44, 45], and the full-field motions of small-scale and full-size engineering structures [41, 46].

The focus of this article is to augment the current nonlinear dynamic test methods with full-field measurement to improve the identification of the nonlinear properties. The primary objective of this paper will be three investigations: 1) how to augment full-field DIC data in nonlinear system test techniques, with a particular focus on the spatial as well as temporal distributions of the dynamic properties of the system, 2) how to select a test technique for a specific nonlinear structure (e.g., a jointed structure) by considering its advantages and deficiencies, and 3) how can the DIC data be used in identifying the modal interaction in jointed structures. Details about the experimental setup, the test specimen, and the data processing procedure are presented in Section 2. As this is a videography-based measurement on a beam with free boundary conditions, constraints are attached as the node point to ensure that the beam stays in the field-of-view (FOV) of the camera for the vibration experiment. The effect of such constraints on the free-response testing and comparison of the results from different test methods using accelerometers are shown in Section 3. In Section 4, the experimental studies using video-based data are conducted to track the evolution of mode shapes with response levels. Additionally, modal interaction behaviors of the test specimen are studied. Finally, the conclusions are given in Section 5.

2. Experimental Setup

Four different types of tests are conducted during the series of experiments, which are listed in Fig. 1. Both free and forced vibration experiments are used to assess which testing strategies can benefit the most from DIC data. In the free vibration experiments, shaker ringdown tests excite only one particular mode with significant vibration amplitude; by contrast, impact hammer tests excite multiple modes. In the forced vibration experiments, FRFs are obtained by force-control and amplitude-control stepped sine testing. The acceleration and displacement response is recorded for all experiments using a set of accelerometers and high-speed digital cameras.

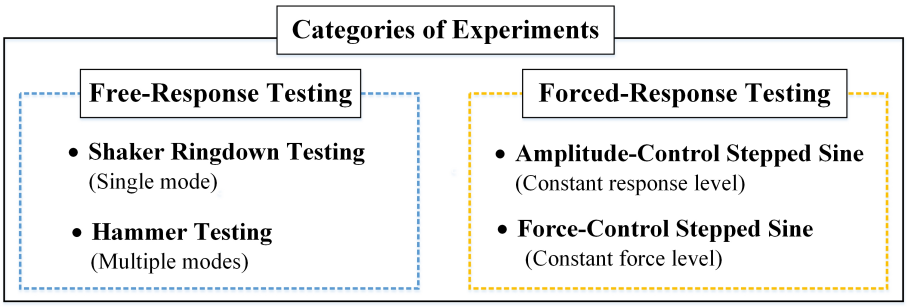

Figure 1: Overview of the different types of experiments.

2.1. Specifications of the Test Specimen

The half Brake-Reuß beam (HBRB) shown in Fig. 2 (a) is a modification of the Brake-Reuß Beam (BRB) [47], in which the width of the BRB is reduced by half in order to decrease the stiffness in the lateral bending direction (i.e., bending in the Y direction; this also reduces the natural frequencies of interest) so that the vibration amplitude can be increased. This modification

in geometry is chosen to improve the functionality of the video-based data acquisition, which measures displacement and is limited by the frame rate and resolution of the camera. The HBRB contains a three-bolt lap joint and is manufactured using wire electrical discharge machining, with the interfaces ground to a 10 μm finish. The geometric properties of this beam are given in Fig. 2 (b) and (c). Aspects including surface curvature, surface roughness, residual stress, prestress, and wear all contribute to the uncertainty of the dynamic characteristics of the jointed structures, which can be found in [2, 47]. To ensure the consistency and repeatability of the experiment, the HBRB is assembled using the process outlined in [48], which is also briefly mentioned as follows. A constant gap in the axial (X) direction is maintained using a 0.35 mm thick shim along the edges of the beam halves to ensure accurate alignment of the interface. The beam halves are bolted together with three stainless steel 5/16"-24 bolts, where the torque for each bolt is the same. The bolts are first tightened to 70% of the desired torque level using a torque wrench in the order of middle, right, and left, and then to the full level in the same order. The boundary conditions of the beam are approximated as free-free, which is achieved by hanging the beam using fishing lines at the two ends of the beam (0.5" from both ends) as shown in Fig. 4 (b). Since the assembly process (specifically, disassembling and reassembling) may affect the dynamic properties of the system, the nonlinear characteristics of the system are measured (via impact hammer tests) every time that the beam is reassembled in order to compare these characteristics across all experiments and to ensure consistency before undertaking a longer set of experiments. Additionally, in order to assess the condition of the beam after an experimental campaign, impact hammer tests are also performed before disassembly in order to quantify any changes in the system due to wear or degradation [49].

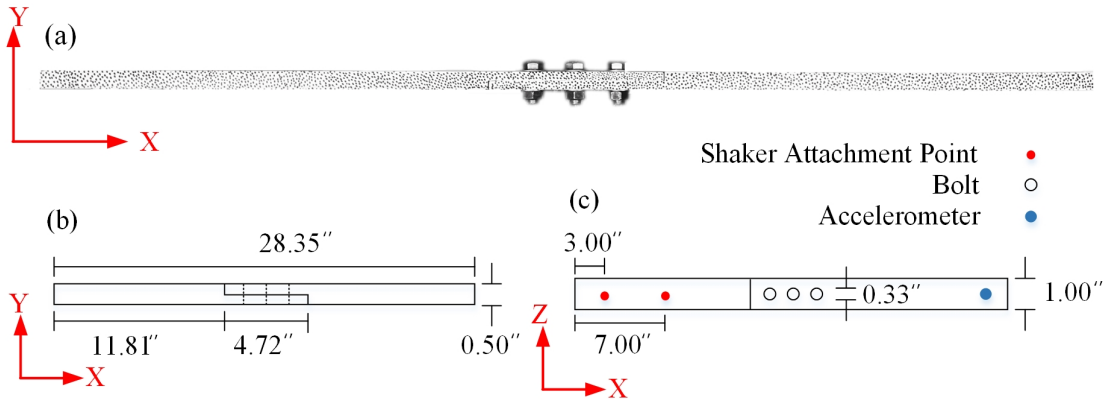

Figure 2: The geometry of the HBRB, shown are (a) the photo of the HBRB, (b) the top view of the HBRB, and (c) the front view of the HBRB.

2.1.1. Linear Modal Properties

A series of linear modal tests are conducted for the specimen with three different torque levels of 10.2, 19.6, and 23.7 N·m. In each of these cases, only one accelerometer is used, which is attached at 1" from the right end of the beam. A roving hammer test is performed with 29 excitation points uniformly spaced 1" apart in the axial direction along the midline of the beam, with a low impact level in the range from 70 to 90 N. The identified natural frequencies and damping ratios obtained directly from the FRFs of the data for the three different torque levels are shown in Table

1. Consistent with measurements of other jointed systems [2, 47], the natural frequencies increase with the torque level, and the damping ratios decrease with torque level. Figure 3 shows the first three mode shapes for the 19.6 N·m bolt torque; no appreciable difference in the first three mode shapes are observed for the three different torque levels. Even though the beam has a geometric discontinuity at the joint location, it is difficult to discern this from the measured data. This is contrasted with the video-based data in Section 4.3.1.

Table 1: The natural frequencies f, in Hz, and damping ratios ξ, in %, of the HBRB at a low excitation level.

Torque level (N·m)	**Mode 1**		**Mode 2**		**Mode 3**	
	f_1(Hz)	ξ_1(%)	f_2(Hz)	ξ_2(%)	f_3(Hz)	ξ_3(%)
10.2	80.31	0.20	290.52	0.07	580.91	0.10
19.6	83.82	0.11	299.99	0.05	589.48	0.05
23.7	84.28	0.07	300.25	0.05	590.15	0.05

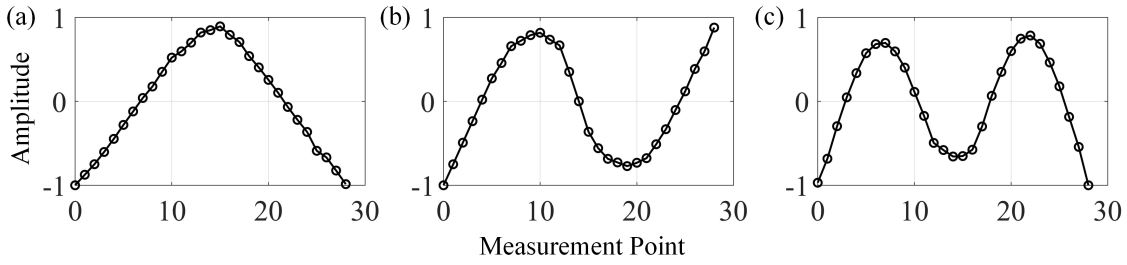

Figure 3: The first three mode shapes of the HBRB from roving hammer testing at a low impact level, shown are (a) mode 1, (b) mode 2, and (c) mode 3.

2.2. Video Acquisition Setup

Two high-speed cameras (Photron Mini UX100) are used to acquire the video data of the jointed beam during dynamic excitation. The experimental setup is shown in Fig. 4. The beam is suspended horizontally from a fixed bar using fishing lines connected to bungee cords with a total length of 1.65 m to simulate free-free boundary conditions. The swing frequency is approximately 2.5 Hz, which is significantly lower than the first natural frequency (80Hz) of the beam. For the hammer tests and shaker ringdown tests, in order to improve the performance of the video-based data acquisition, additional constraints (bungees) are added to the beam. The effect of the constraints on the system is studied in detail in Section 3.1. Since the beam vibrates in the X-Y plane in Fig. 4, the cameras are positioned and aligned perpendicularly above the plane to capture the responses of the beam. The cameras are positioned such that the pixel to actual physical displacement conversion is consistent for all of the points on the beam (i.e., the plane of the beam and plane of the camera are parallel). A level is used to ensure that the beam and camera are parallel, and the distortion from the camera and lens is checked through 2D calibration via a Matlab toolbox called Camera Calibrator [50, 51]. Two cameras are placed 1 m above the top surface of the beam with 35 mm focal length lenses such that each camera records slightly more than one-half of the beam. For proper illumination, two 1000-watt halogen bulbs are placed symmetrically at the two sides of the beam. The sampling frequency is kept as 8000 frames per second (FPS) or higher

with the camera shutter speed of 16 μs to capture the high-frequency vibration. The cameras are synchronized by using a built-in triggering mechanism that starts recording for both cameras simultaneously. Using the videos from both of the cameras, the vibration profile of the whole beam can be obtained by stitching the two images obtained from the two cameras. The displacements recorded in the video are in pixels, which are converted to physical units by a conversion factor that is calculated by taking the length of the beam as the reference dimension and dividing the length by the number of pixels that the beam spans in the image. The measurement uncertainty from the DIC code and environment is evaluated through static analysis in Section 4.1, following which the noise level for the current test setup and displacement extraction code can be quantified. Responses at or below the noise threshold are discarded from the analysis.

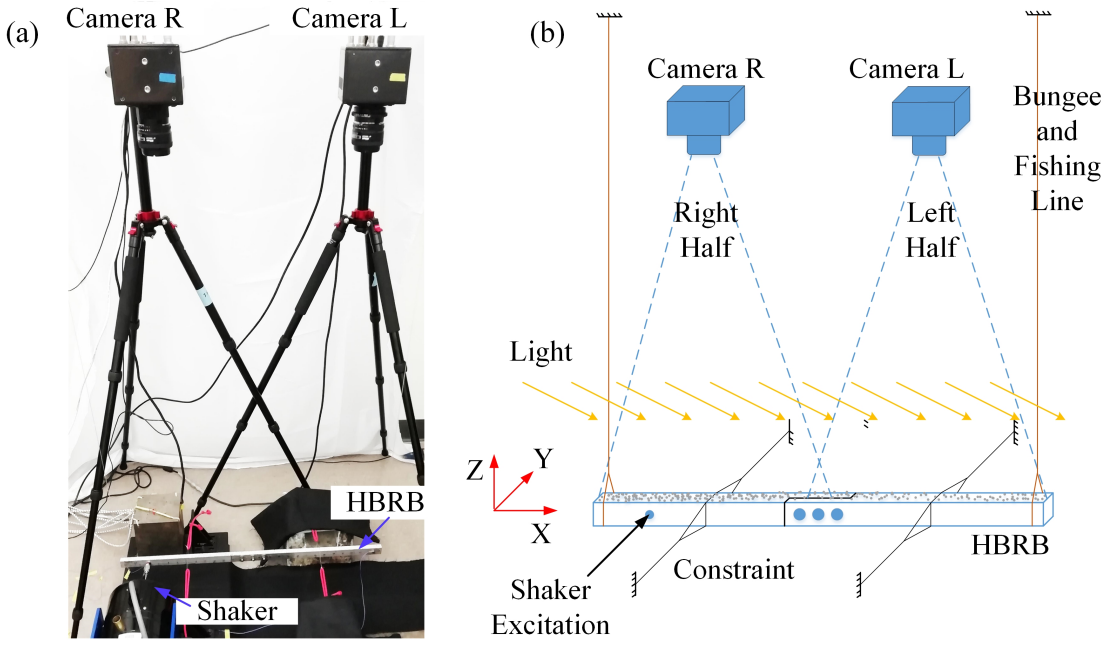

Figure 4: The test setup with the high-speed cameras. Shown are (a) the photo of the test setup, (b) the schematic diagram of the test setup.

As an example, one image pair from the left and right cameras are shown in Fig. 5. The images from the high-speed cameras are grayscale images with a depth of 12 bit. For better use of the limited memory of the high-speed cameras (16 GB) in capturing the full beam, the FOV of the cameras is fixed as 1280×312. From Fig. 5, the two images have an overlap area of the middle bolt to ensure that the spatial motion profile of the whole beam can be reconstructed from these two independent images.

2.3. Specifications for Images Prior to Post Processing

To use DIC to measure the displacement of the beam, a speckle pattern is needed [52]. The top surface of the beam is painted with white matte paint as a primer. Black dots are marked randomly with a sharpie on the top surface of the whole beam, and each dark speckle spans three to five pixels [52]. Such speckles are drawn in a random manner in terms of spatial location as well as size to make all of the small image patches unique, which helps the DIC method to track properly. The recorded images are processed by the DIC software 'Digital Image Correlation Engine' (DICe) [53]

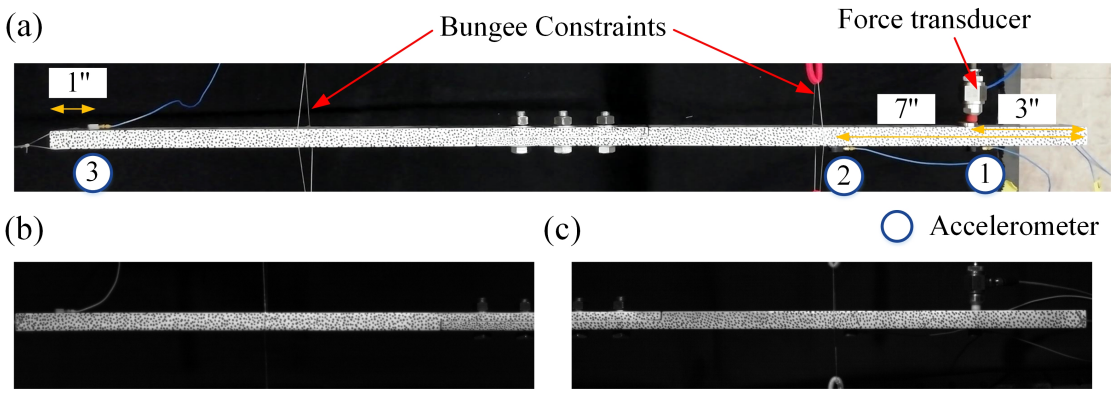

Figure 5: The images of the test beam, shown are (a) the top view of the HBRB, (b) the image from the left camera, and (c) the image from the right camera. The blue circles with numbers inside in (a) refer to the accelerometers.

to extract the displacement of the beam. The displacements are measured by creating overlapping square windows (or subsets) on the area of interest and tracking the motions of the subsets via image correlation. The displacement responses extracted by image correlation are the average responses of the subsets, which are commonly referred to as the responses at the center points. For a higher spatial resolution in the measurements, a smaller subset size is desirable; however, smaller subset sizes will bring about uncertainty during the image correlation and may cause more error for the extracted responses. In all of the tests, the length of the subset was set as 21 pixels (shown in Fig. 6; as each subset is square, this results in a total of 441 pixels inside the subset), and the overlap between the two subsets was set as 11 pixels. In Fig. 6 (a), the subsets in red were selected for DICe to calculate the displacement along the dashed red line. If the subsets are placed along the two sides of the interface, then the joint behaviors can be measured. In the previous work of the authors [45, 44], the FOV is focused on the jointed interface itself to measure the relative tangential and vertical motions of the interface under the dynamic excitations. Here, however, the focus is on the global motion of the system, and thus a coarser FOV is used compared to previous work.

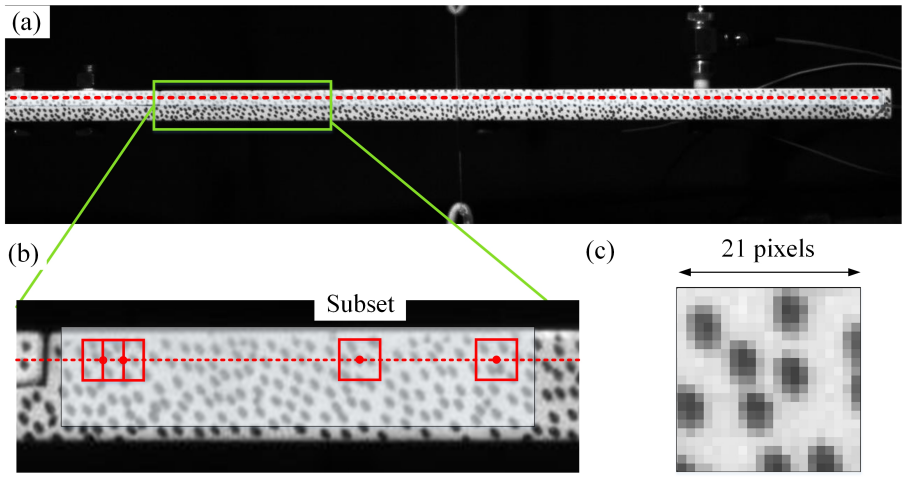

Figure 6: DIC settings for the measurements. Shown are (a) measurement locations on the beam, (b) a zoom-in of the beam, and (c) a subset.

2.4. Free Response Testing Experimental Setup

For the free-response testing, extra constraints (bungee cords) are added symmetrically at the two sides of the beam to reduce the rigid body motion of the free-free beam. This is necessary for the subsequent video-based measurements; without the additional constraints, the specimen would move in and out of the FOV of the cameras (see the narrow FOV in Fig. 5 (b) and (c)). The selection of the locations of the additional constraints and their effect on the system dynamics is discussed further in Section 3.1.

2.5. Shaker Ringdown Testing

The experimental setup for shaker ringdown testing is shown in Fig. 5 (a). In addition to the cameras, the acceleration responses and input forces (through a 267 N shaker) are recorded by three accelerometers and a force transducer, respectively. The shaker is controlled by the signal source inside the data acquisition system. In the experiment, the system is excited by a sinusoidal signal that matches the resonant frequency of a target mode for a particular response level. When the steady-state response is reached, the external force is removed from the system to observe the free decay in that corresponding mode. Then, the amplitude-dependent frequency and damping ratio curves can be estimated directly for that mode. In this case, a shaker is used to excite a particular point of the HBRB, and when the beam reaches its steady-state, which can be observed from the acceleration measurements, the stinger completely detaches from the beam, allowing the vibration energy in the beam to decay freely.

The challenging part for the shaker ringdown testing is to separate the shaker and the test specimen physically since the shaker adds mass and extra damping to the test structure. For large systems [12], the shaker and system are not decoupled based on the assumption that the shaker does not appreciably contribute to the system's dynamics. However, for the jointed HBRB specimen, the shaker adds a significant amount of damping to the system due to its electromagnetic mechanism and its relatively large size compared to the test specimen. Hence, a new setup, inspired by [54], is devised that completely detaches the stinger from the beam specimen.

2.5.1. Shaker Decoupling Mechanism

The shaker decoupling mechanism consists of preloading the stinger against the beam instead of rigidly connecting it. With a large enough preload, the stinger does not lose contact with the beam during dynamic excitation. As shown in Fig. 7, the stinger is attached to the force transducer, which in turn is attached to a rubber impact hammer tip. At the point of contact with the beam, there is a tapped hole for forced-response shaker testing; a cap used for impact testing in similar situations is fixed to this hole so that both the shaker ringdown testing and the forced-response shaker testing are able to excite the system at the same location. The value of the DC offset is chosen such that the stinger can retract 1.5 cm, which is sufficient to ensure that the stinger assembly does not contact the beam during the subsequent ringdown. To decouple the stinger and test specimen, the DC offset of -4 V is applied to the shaker control signal. To minimize disruption to the vibration of the specimen, the DC offset is applied at a phase of 360 degrees where the beam has the maximum velocity towards the opposite direction. This phase was determined as experiments deduced that it had a minimal influence compared to other candidate phases. This process is further described below.

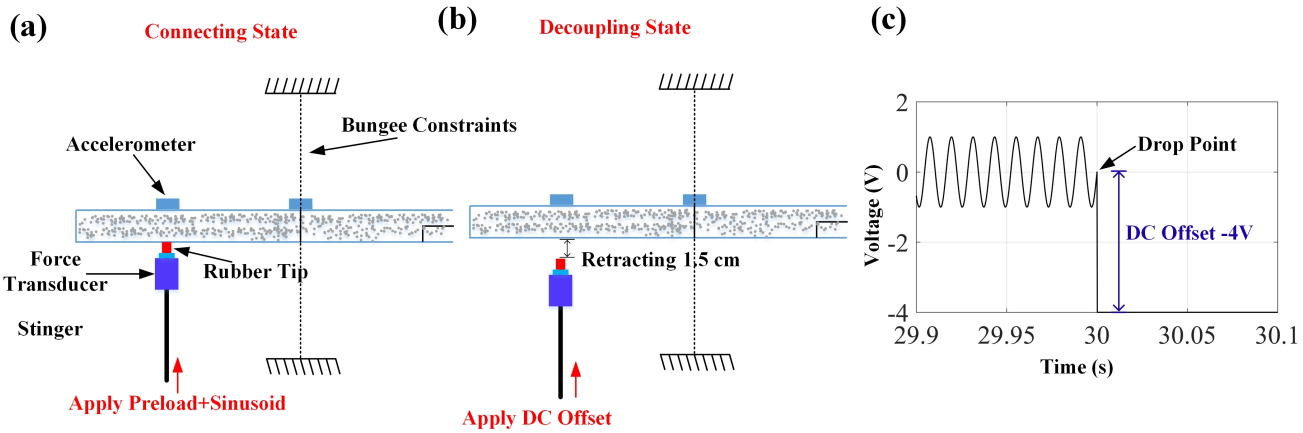

Figure 7: The decoupling mechanism of the stinger and the beam, shown are (a) the state with preload and sinusoidal excitation added, (b) the decoupling state where the stinger retracts, (c) the applied DC offset signal.

2.5.2. Shaker Ringdown Methodology

The steps for conducting shaker ringdown testing are shown in Fig. 8 and are summarized as:

- **Step 1: Estimation of natural frequency**

  The approximate natural frequencies of the system are searched at a particular response level (e.g., Root Mean Square (RMS) of 5 g) using random broadband excitation. The modal parameters within the target frequency range are identified through the obtained FRFs using linear modal analysis principles.

- **Step 2: Driving point phase difference evaluation to determine the precise natural frequency**

  Next, the shaker is driven with a fixed sine signal set at the estimated natural frequency and the target amplitude. The response of the accelerometer at the same location as the excitation point is recorded to estimate the phase between the force and excitation. For estimating the phase difference, the Cross Power Spectral Density (CPSD) (the Fast Fourier Transform (FFT) of the correlation function) is used, which can show the phase difference of two sinusoids directly. As shown in Fig. 8 (b), the phase difference between the force and response is recorded where the absolute value of the CPSD is a maximum. Such phase difference should be close to $-90°$ if the sinusoidal forcing function frequency is close to the actual natural frequency.

- **Step 3: Adjustment of excitation frequency if the driving point phase difference is out of a preset threshold**

  Due to the amplitude-dependent properties of the jointed structure, the identified frequency from random excitation testing is often not the exact natural frequency at the target excitation level. In this case, the phase difference is not close to $-90°$, and so the excitation frequency is adjusted by a frequency step (e.g., increments of 0.1 Hz during the test). When the phase difference is within the threshold, which is set as $\pm 5°$ around $-90°$, the adjustment procedure stops. Fig. 8 (b) shows that the phase difference between the force and the acceleration signal is $-91.23°$ which is within the threshold limit. After completion of this step,

the obtained frequency and target excitation level is used for the input signal generation for the shaker ringdown test.

- **Step 4: Detachment of shaker and recording of ringdown data**

  After finding the excitation frequency at the desired response level, the DC offset signal is generated and applied to the structure. As shown in Fig. 8 (c), the DC offset signal contains two parts; in the first 30 s, there is a sinusoidal signal with frequency obtained from Step 3, and the last 30 s consist of the constant DC part, which does not have any motion. As discussed above, the stinger is preloaded against the beam, and for the first 30 seconds, it is used to transmit the shaker excitation to the beam such that the beam reaches a steady-state. During this time, as the beam is constrained at the node points, the force transducer is monitored to ensure that the stinger never loses a significant portion of its preload and is able to maintain contact for the whole 30 seconds. The duration of 30 seconds is chosen to ensure that the specimen achieves the steady-state response corresponding to a particular target mode for that response amplitude level. At the designated time (30 seconds), the DC offset is applied to the shaker's excitation signal, resulting in the stinger being decoupled from the beam and being retracted 1.5 cm such that it never contacts the beam for the remainder of the experiment, which allows the vibration in the structure to decay freely with a single-mode component. The example response of the accelerometer at location 1 (see Fig. 5 (a)) is shown in Fig. 8 (d). Just prior to the separation of the stinger from the beam, the two cameras are triggered to capture the free responses of the whole beam for about 4 seconds. In this experiment, the excitation force-time history, the accelerometer data, and the video is recorded. The sampling frequency for the video data is 5000 Hz for mode 1 and 8000 Hz for modes 2 and 3, and similarly, the sampling frequency for the accelerometer data is 6400Hz for mode 1 and 12800Hz for mode 2 and 3. From this ringdown response, the instantaneous frequency and damping ratio of the target mode can be calculated.

This procedure is followed to obtain the free responses of all of the first three modes. To excite the target mode sufficiently, there are some studies to detect the optimal excitation location using Fisher information [55] and modal force vector [56]. In this paper, the optimal excitation location of the beam for each mode is estimated using the method proposed in [56]. This algorithm determines the optimal location of the shaker to increase the vibration amplitude of a particular mode. According to [56], for exciting modes 1, 2, and 3, the shaker should be attached at 3", 7", and 7" from the right side of the beam, respectively.

2.6. Impact Hammer Testing

Hammer testing is a convenient and practical way to obtain the dynamic properties by analyzing the responses after the hammer impacts the test specimen. The impact is a broadband excitation, whose frequency range depends mainly on the material of the hammer tip. For this experiment, the tip is made of plastic and has an effective excitation frequency range of 0 to 2800 Hz. The same experimental setup used for the shaker ringdown is used for the hammer testing, except that the shaker and stinger assembly is completely removed and never engages the HBRB.

The impact location is the same as the shaker attachment points used in the shaker ringdown testing (3", 7", and 7" from the left side for mode 1, 2, and 3 respectively in Fig. 5 (a)), and the excitation levels are 100, 300, and 700 N (though the 700 N case is not used in all experiments in

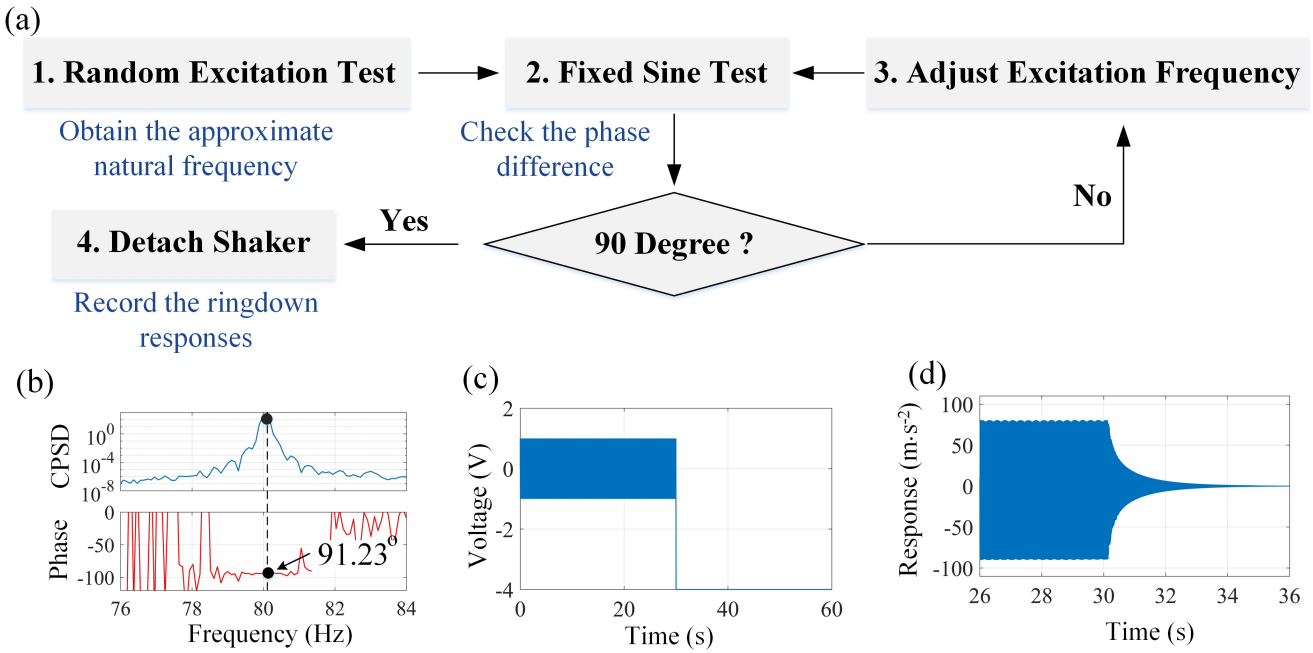

Figure 8: The flow chart of the shaker ringdown testing, shown are (a) the whole procedure for the shaker ringdown testing, (b) the cross-spectrum of the response and input force, (c) the input signal to the excitation system for detaching the shaker and test specimen, and (d) the free response of the system.

order to avoid excessive wear of the system) for mode 1, 2, and 3, respectively. Two repeats are conducted for each excitation level. The cameras capture the response of the entire beam from the initial impact until the beam dissipates the impact energy. Note that the camera data from a low excitation level has a relatively low signal-to-noise ratio (SNR) as low pixel-level displacement is not captured properly in the video-based measurement. Therefore, mainly the excitation level of 700 N is used for the hammer tests when the response is recorded by the cameras. The duration of the recording for the cameras is 4.5 s with a sampling frequency of 8000 Hz.

From each hammer test, the response of a single-mode (Fig. 9 (b)) is extracted from the raw acceleration data (Fig. 9 (a)) by reversing the time signal and then using a 4th-order Butterworth bandpass filter (with a bandwidth of 16 Hz) [57, 58]. The frequency-domain response of the filtered response and raw data are shown in Fig. 9 (c). The Peak Finding and Fitting (PFF) method [58] is then used to extract the instantaneous damping and frequency of the system, as shown in Fig. 9 (d) and (e). Due to friction in the joint interface, the natural frequency of the jointed structures decreases with increasing vibration amplitude (exhibiting the softening behavior expected from this type of jointed structure), while the damping ratio increases with the amplitude[2].

2.7. Forced Response Testing

For nonlinear jointed structures, amplitude- or force-control stepped sine testing is an effective technique to obtain the amplitude-dependent properties [14]. The backbone curves of the system can be directly calculated from the measured FRFs at different excitation amplitudes. A key difference between amplitude-controlled and force-controlled experiments is that amplitude-controlled experiments maintain a constant response spectrum, and force-controlled experiments maintain a constant force spectrum. The choice in amplitude- or force-controlled has ramifications for the

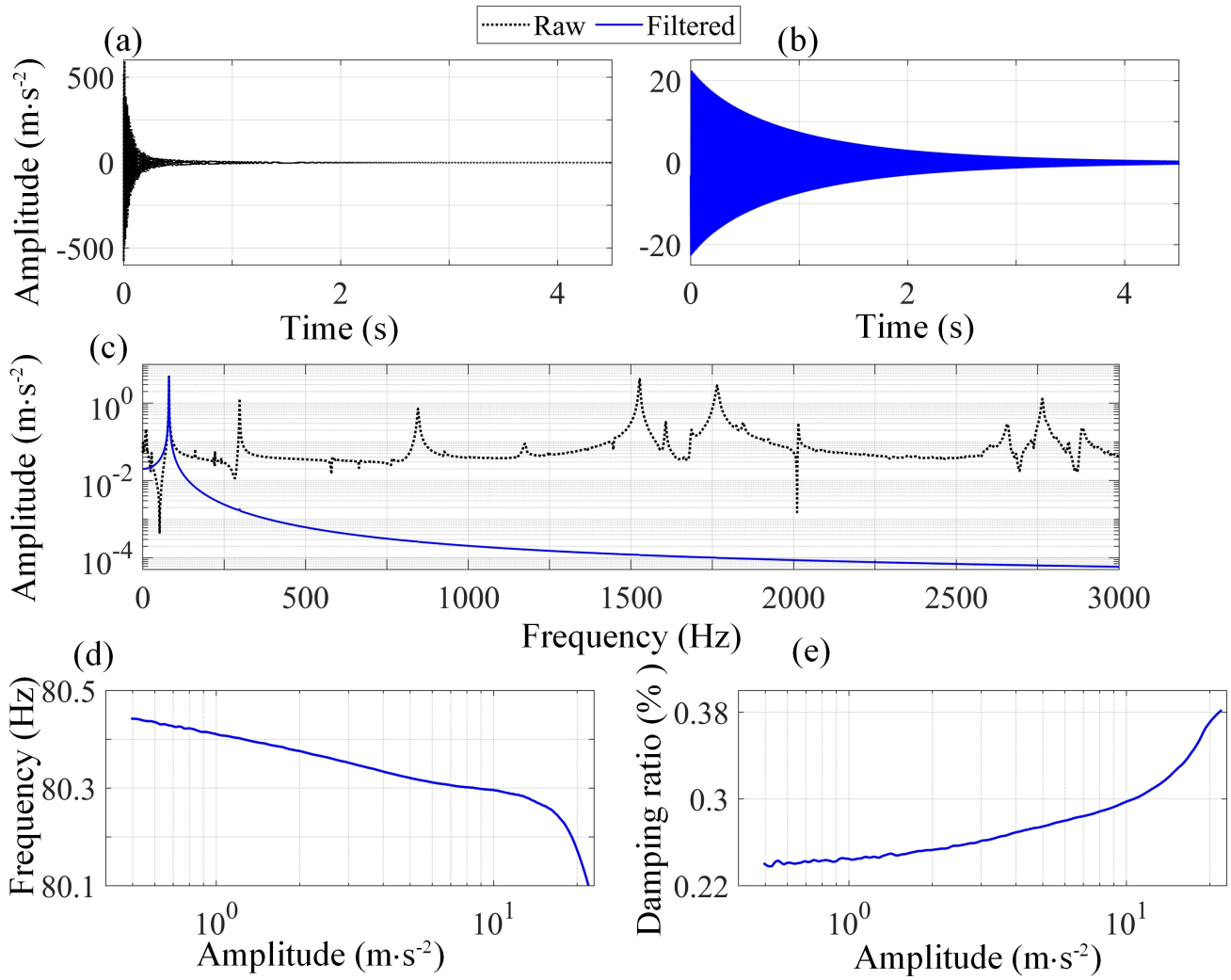

Figure 9: Typical results from hammer impact testing, showing (a) the raw data from the accelerometer, (b) the band pass filtered responses in the time domain, (c) the FFT of both the raw data and the band pass filtered responses, (d) the amplitude-dependent natural frequency, and (e) the amplitude-dependent damping ratio.

extraction of the backbone curves, as is discussed further in Smith et al. [59]. The employed control strategy can be treated as a closed-loop controller, which keeps the response or force level at the given frequency in an acceptable interval by changing the input current for the amplifier. Consequently, the input force may be distorted and contain higher harmonics of the excitation frequency.

The test setup is shown in Fig. 10. The force transducer connects the stinger and the beam through a screw connection. Hence, for these forced vibration tests, no additional constraints are required because the shaker's excitation amplitude is insufficient for the beam to go beyond the FOV of the cameras. Three accelerometers are placed at 1" from the left side, and 3" and 7" from the right free edge to measure the responses. For mode 1, the shaker is attached to the beam at 3" from the right side, which is close to the node point of mode 2 and 3; for mode 2 and 3, the shaker is attached to the beam at 7" from the right side, which is close to the node point of mode 1, to ensure that the energy from the shaker is focussed into the corresponding target mode. During the

test, a step of 0.05 Hz is used, and the specimen is excited for 3 s at each step to reach a steady state.

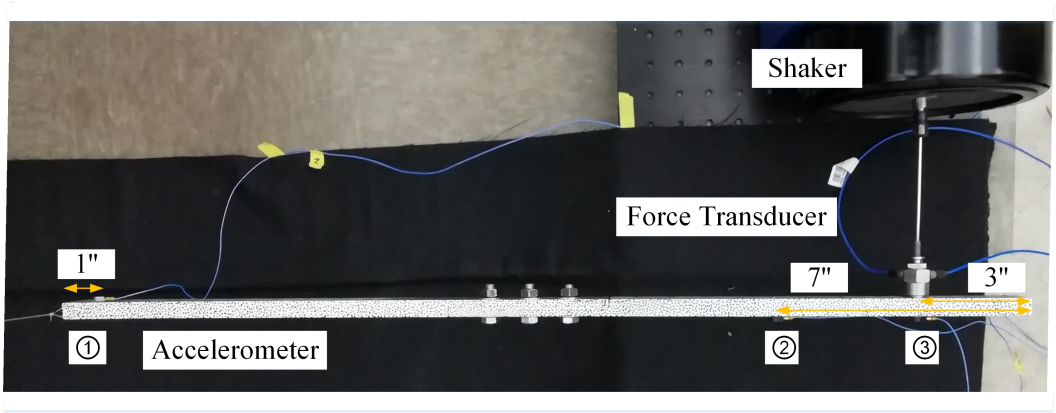

Figure 10: The test setup for the forced response testing.

2.7.1. Amplitude Control

During the amplitude-controlled stepped-sine testing, the driven point refers to the response measurement point with the exact same location as the excitation. The detailed settings for amplitude-controlled stepped-sine testing are shown in Table 2.

Table 2: Settings for amplitude-control stepped sine testing.

Test Mode	Driven Point	Sweep Range (Hz)	Step (Hz)	Controlled Amplitude (g)
1st	Point 3	79.0-81.0	0.05	0.5, 2, 4, 5, 6, 7, 8
2nd	Point 2	294.5-298.5	0.05	2, 4, 6, 8,10
3rd	Point 2	576.8-582.8	0.05	2, 5, 10

The response levels of the driven point and excitation level are shown in Fig. 11 for the amplitude-control stepped sine test. Ideally, the response amplitude of the driven point should be a horizontal line with the set level during each stepped sine test. In Fig. 11 (a), (c), and (e), each dashed line is approximately constant, which means that the response level of the driven point is well controlled during the stepped sine test. For the excitation force, the lines corresponding to the force amplitude drop smoothly at the resonant frequency. The FRFs of modes 1, 2, and 3 for different amplitude responses are shown in Fig. 11 (b), (d), and (e), respectively. These curves are obtained by dividing the response curves by the force curves for each controlled level. As the response level increases, the amplitude of the FRF decreases. Since the amplitude of the FRF is inversely related to the damping ratio, the damping ratio of the structure increases with increasing response amplitude.

2.7.2. Force Control

For the force-control stepped sine test, the experimental setup is the same as that for the amplitude-controlled stepped-sine test. The force-controlled stepped-sine test is conducted from 79 to 81 Hz with a step of 0.05 Hz and force levels of 0.2, 0.5, 1.0, and 1.5 N for mode 1. As

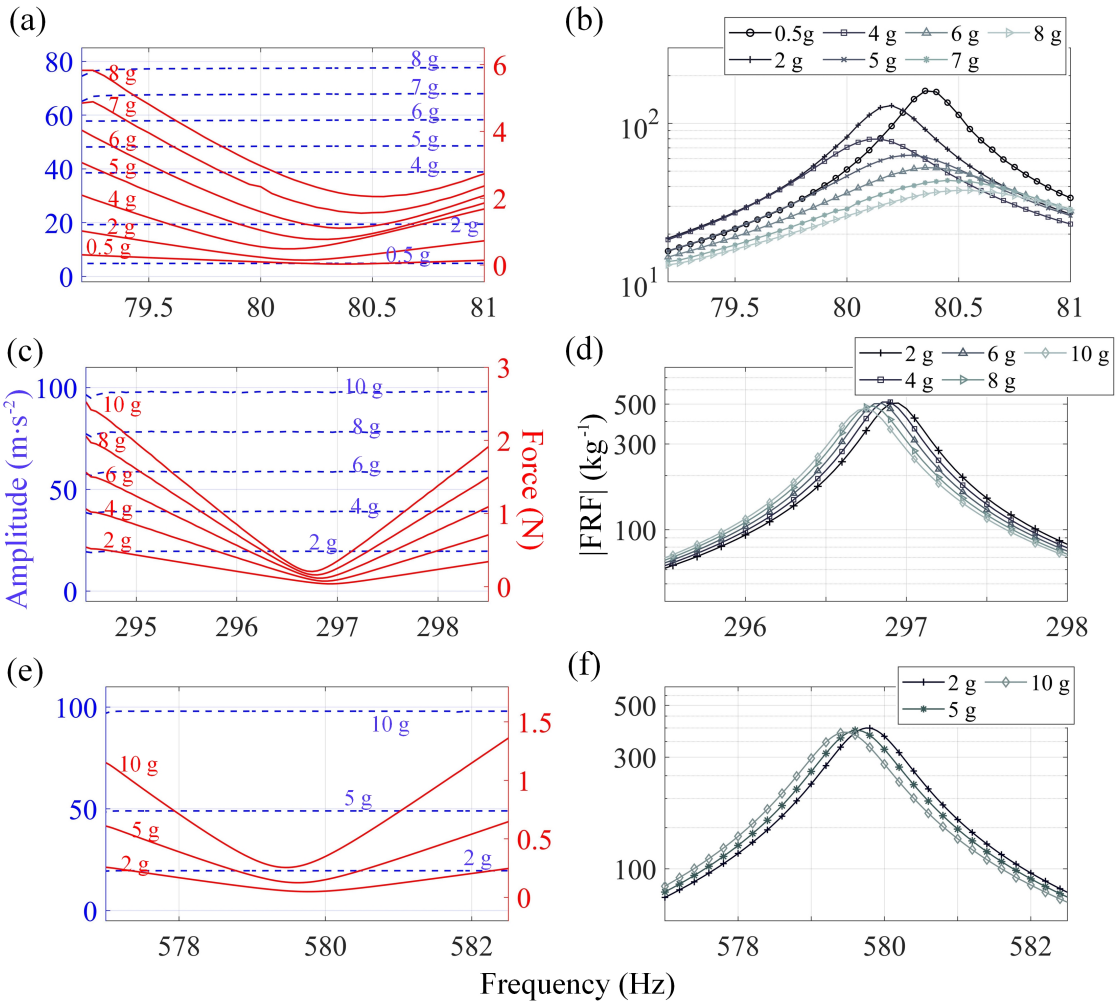

Figure 11: The response levels, excitation levels, and corresponding FRFs during the amplitude-control stepped sine testing, shown are response levels and excitation levels for (a) mode 1, (c) mode 2 and (e) mode 3; the corresponding FRFs for (b) mode 1, (d) mode 2, (f) mode 3. Subfigures (a), (c), and (d) has left y-label as amplitudes in m/sec^2 and right y-label as force in N. Similarly subfigures (b), (d), and (f) has y-label as —FRF— in kg^{-1}. xlable of all the subfigures are Frequency in Hz. The dashed lines represent the response level for the amplitude-control stepped sine. The solid lines represent the excitation force levels.

shown in Fig. 12 (a), the excitation forces (solid lines) maintain almost the same level during the stepped-sine test, while the corresponding responses (dashed lines) show peaks. Compared to the dashed lines in Fig. 11 (a), the solid lines show more fluctuation. Specifically, for the 1.5 N control level in Fig. 12 (a), the lowest amplitude is 1.28 N, and the highest level is 1.62 N. Additionally, the solid red lines, which represent the response levels, are not smooth for this frequency band. In Fig. 12 (b), the height of the FRF decreases with increases in the excitation force level, which indicates an increase in damping for high response levels. Experiments for modes 2 and 3 were not conducted because of the clear advantage presented by the amplitude-controlled experiments, and because it is also very difficult to maintain a constant force level for the higher modes.

Amplitude-controlled or force-controlled stepped-sine testing is much more mature compared with shaker ringdown testing. However, in practice, this method may not be suitable for low response levels because the force required to excite the low-amplitude responses at the resonant

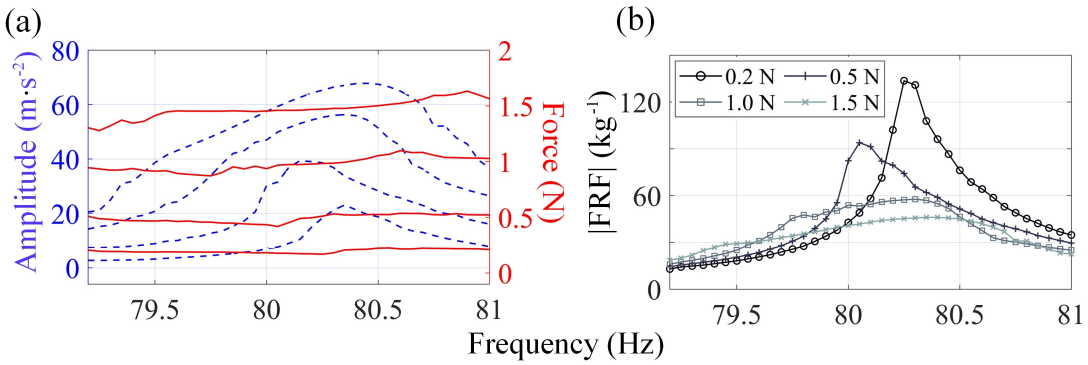

Figure 12: The response levels, excitation levels, and corresponding FRFs during the force-controlled stepped-sine, shown are (a) response levels and excitation levels, and (b) the corresponding FRFs. The dashed lines represent the response level for the amplitude-controlled stepped-sine. The solid lines represent the excitation force levels.

frequency may be contaminated by noise. Compared with force-controlled stepped-sine testing, the amplitude-controlled stepped-sine testing is more stable, and the measured force and response amplitude curves are much smoother. Due to these issues, only amplitude-control stepped sine testing is considered further.

3. Preliminary Analysis

The first set of experiments are analyzed without video data in order to characterize the system and to provide a basis for validating the video-based measurements. These experiments use accelerometer data to measure the response of the system.

3.1. Constraint Analysis

The first analysis focuses on determining if the additional constraints (to keep the beam within the FOV of the cameras) significantly affect the dynamics of the beam. For linear systems, adding constraints on the node points of any particular mode will not have any effect on that mode. However, as the HBRB is a nonlinear system, the mode shapes change with amplitude, and bifurcations in the dynamics may lead to modal interactions, including internal resonance and mode conversion. To study the effect of the constraints on the system and to find the placements that minimize these effects, hammer tests with different constraint locations on the beam were conducted.

The HBRB with each bolt torqued to 20 N·m is considered for this experiment. Figure 13 shows the test strategy for the beam. The excitation location and the accelerometer are placed 1" from the left end of the beam. The elastic bungees are attached to the beam symmetrically at a distance L from both the left and right sides. Here, L ranges from 1" to 13" with a step of 2". Hammer testing is conducted for each of the specified constraint locations, and the responses from the first three modes are extracted from the response. The backbone curves and the damping-amplitude curves measured for the different constraint locations are compared against the measurements from the unconstrained system.

Figure 14 shows the backbone curves and damping-amplitude curves for modes 1, 2, and 3. Each of the curves in these figures is obtained from the response with a different constraint location.

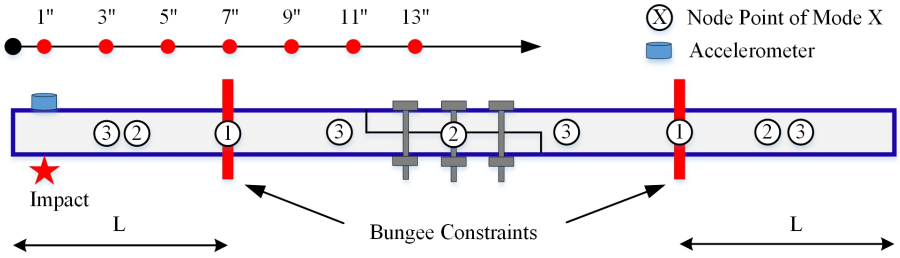

Figure 13: The experimental strategy of bungee constraints. The circles with numbers inside are the locations of the node points.

For mode 1 (see Fig. 14 (a) and (b)), compared with other constraint locations, the curves with the constraint at 7" match well with that of the free-free boundary condition where there is no additional constraint attached to the beam. This makes sense as 7" is the node point of mode 1 (see Fig. 13); hence, constraining at 7" from both of the ends has the least effect on the frequency and damping ratio curves of mode 1. For the other constraint locations, the response exhibits much higher damping than for the optimal constraint location. The same conclusion for the frequency, as well as damping ratio, holds for the results of modes 2 and 3. Since the node point of mode 2 is between 3" and 5", the backbones curves and damping-amplitude curves of constraints at these two locations are close to that without constraints. According to the results above, the constraint at the node point of a mode has the least effect on that mode. The applied constraint location for the free-response testing is shown in Table 3.

Table 3: Constraint location for the three modes.

Mode Order	1	2	3
Constraint Locations	7"	3.5"	3"

3.2. Result Comparison

With the optimal constraint locations identified, the next step is to compare each of the different testing methods. The amplitude-dependent frequency and damping ratios of the first three modes are extracted from the hammer tests with no constraint, the hammer tests with optimal constraint, the shaker ringdown tests with optimal constraint, and the amplitude-controlled stepped-sine tests. The torque level for each bolt is 10 N·m. The results are shown and compared with each other in Fig. 15.

The amplitude-dependent frequency and damping ratio curves are consistent with each other for all three modes in Fig. 15. Thus, the optimal constraint has little effect on the free-response testing, and all of the test methods are valid to extract the nonlinear properties. For the first mode, the amplitude-controlled stepped-sine tests and the shaker ringdown tests are able to excite the response to a much higher amplitude than the hammer tests. Moreover, the damping ratio shows a variation from 0.72% to 0.21% with amplitude dropping from 80 $m{\cdot}s^{-2}$ to 0.1 $m{\cdot}s^{-2}$, which is much higher than that of the second and third modes. Therefore, the nonlinearity has a smaller effect on the second and third modes than on the first mode.

Hammer tests are a good approach to obtain the nonlinear properties and their trend (softening or hardening) at relatively low amplitudes. In contrast, the amplitude-controlled stepped-sine tests

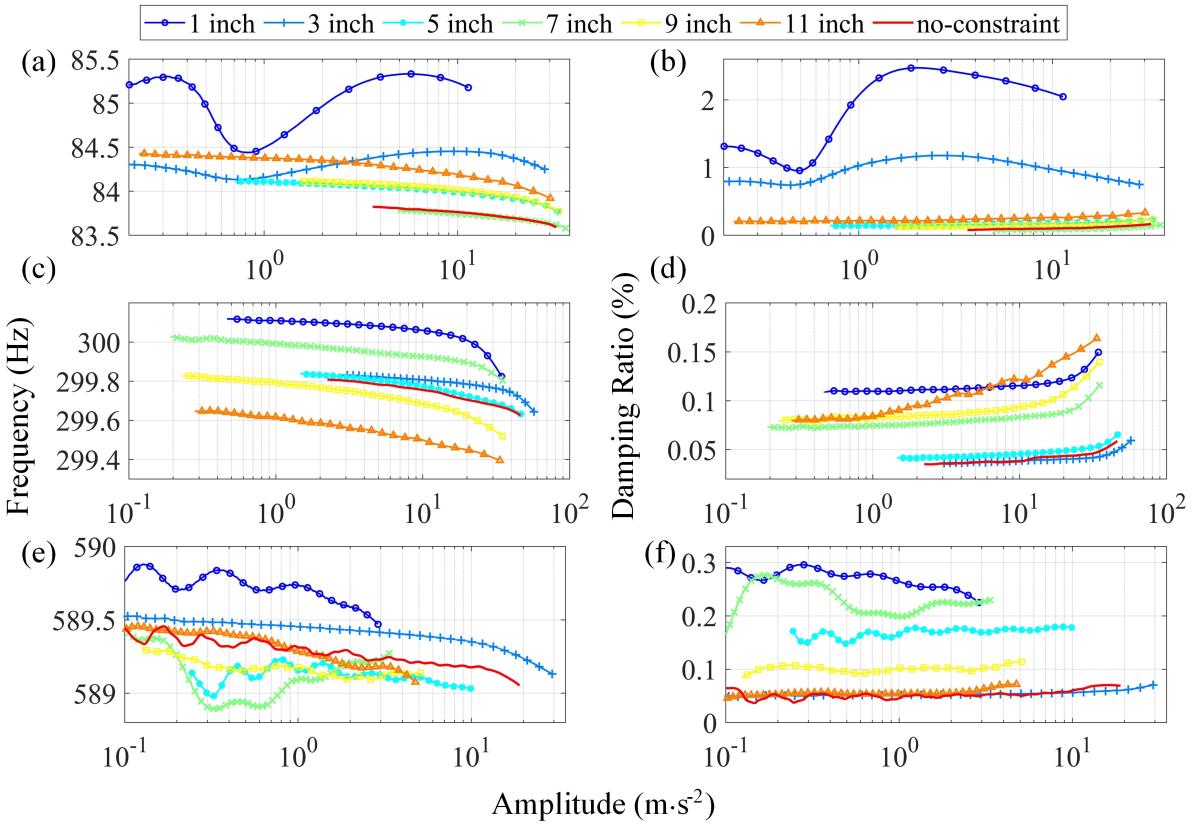

Figure 14: Backbone and damping-amplitude curves for different constraint locations, shown are backbone curves for (a) mode 1, (c) mode 2 and (e) mode 3, and damping-amplitude curves for (b) mode 1, (d) mode 2 and (f) mode 3.

show advantages in obtaining properties at high response levels but may not be suitable for the low response levels due to inaccuracies in the measurements of the force at low amplitudes, especially at the resonant frequency. The shaker ringdown tests show advantages in both exciting the target mode to high levels and recording that mode at low levels. Since a sinusoidal excitation is used, which has energy in a narrow band, the target mode (especially the first mode) can be excited to a level much higher than that from hammer tests. When the beam is separated from the shaker, the free decay response can be recorded from a high to a low response level (i.e., the noise level), which probes the nonlinearity in a wide range of response amplitude.

4. Experimental Study Using Video Data

The responses measured with accelerometer data in Section 3 are used to narrow the range of experiments conducted with videography. The process of recording, transferring to a computer, and processing the video data with the subsequent DIC analysis is time-consuming, so it is prudent to narrow the number of experiments conducted with videography. DIC data can provide dense spatial information of the beam; hence, it is uniquely suited to provide information about the entire mode shapes of the beam (as opposed to measurements at discrete points). An alternative approach might be the use of a scanning laser Doppler vibrometer (LDV) [27, 41]; however, an LDV is only able to measure normal motion, and the present study is concerned with planar motion.

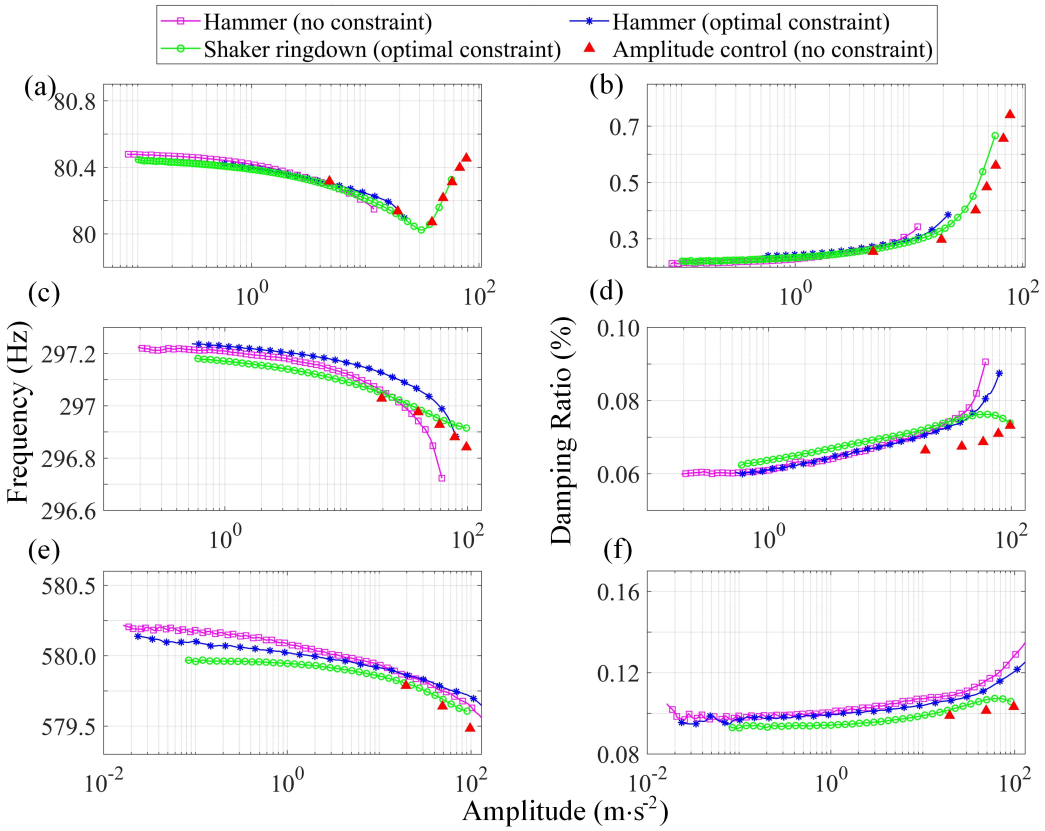

Figure 15: Backbone and damping-amplitude curves from different tests, shown are backbone curves for (a) mode 1, (c) mode 2 and (e) mode 3, and damping-amplitude curves for (b) mode 1, (d) mode 2 and (f) mode 3.

4.1. Noise Level Test

Prior to using the DIC data for any vibration test, the noise level for the camera-based measurement should be quantitatively assessed to evaluate the data quality. Hence, for this experiment, the HBRB is laid flat such that it is motionless. Without any excitation, the measured responses are ambient noise signals of the whole measurement system, including the camera (and its fan), tripod, light source, and the DIC method. Approximately 200 measurement points along the beam are tracked by the DIC technique. The signal is recorded for 2 s with a sampling frequency of 5000 Hz.

The time histories of all of these measurement points are shown in Fig. 16 (a). Even though the beam is static, all of the points show that the response varies within ± 0.02 pixels in the time history, which is considered to be the noise for this measurement system. The frequency content of the noise responses is shown in Fig. 16 (b). Two dominant peaks are observed at 120 Hz and 146.2 Hz, which are separated from the natural frequencies of the test beam. The peak at 120 Hz is due to the electrical noise, and the peak at 146.2 Hz is due to the rotation of the fan inside the high-speed cameras.

For proper quantification of the noise level of the measurement system, statistical analysis is conducted using the DIC data. The probability density function (PDF) of the noise signal is represented by the histogram of the recorded signals, which is also fitted by Gaussian distribution in Fig. 16 (c). From the cumulative distribution function (CDF) of this noise profile, according

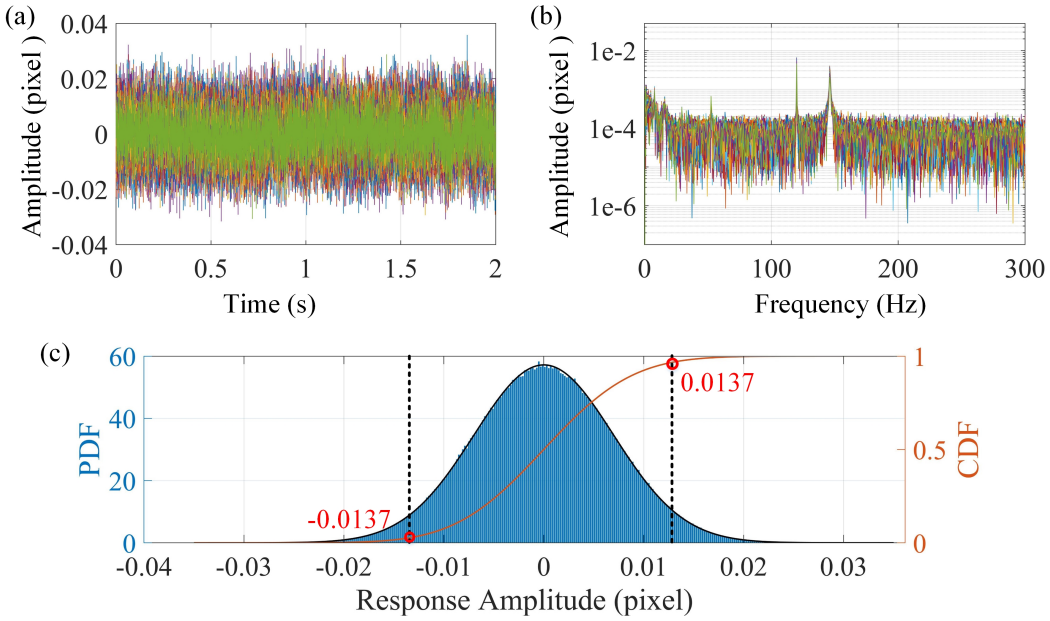

Figure 16: The static responses in time and frequency domain, shown are (a) time history of noise responses, (b) frequency content of noise responses, and (c) noise level determination from DIC data.

to the 95% confidence interval (dashed lines), the noise level is found to be 0.0137 pixel which is 3.9 μm in terms of the physical unit (as 1 pixel equals to 0.285 mm, details can be found in Section 2.2). Hence, if the response level is below 3.9 μm, the raw data is not valid for further analysis.

4.2. Validation of DIC Data with Accelerometer Data

To show that the responses obtained from DIC in these experiments are accurate enough for characterizing the nonlinearity, the instantaneous frequency and damping ratio curves using the DIC data are compared with the curves obtained from the accelerometer data. For this comparison task, test results from a shaker ringdown experiment are used, where the bolt torque used to assemble the HBRB is 10 N·m.

Displacement time histories of the beam are recorded in a dense manner, i.e., 205 measurement points along the beam, which is shown in Fig. 17 (a). Owing to the high spatial resolution of the DIC measurement, the motion of the whole beam can be reproduced from this figure. Since the beam is released at the resonance frequency of the 1st mode, the mode shape of the 1st mode can be seen from any time instant of the response. The recorded response from the accelerometer (accelerometer 1 in Fig. 5) is shown in Fig. 17 (b), and the response from DIC at this location is shown in Fig. 17 (c). Since the SNR decreases with the decay of the response, the recorded response from DIC is truncated at 3.5 s. The low-frequency oscillation seen in Fig. 17 (c) is due to the rigid body sway mode of the constrained system (as acceleration scales with frequency squared, this is not visible in the acceleration data).

The amplitude-time-frequency curve and amplitude-time-damping curve are extracted from the accelerometer data (see Fig. 17 (b)) and DIC data (Fig. 17 (c)) at the same location of the beam. The responses are reverse filtered [57] by a 4th-order Butterworth bandpass filter, and then the filtered response is used to extract the instantaneous frequency, damping ratio, and

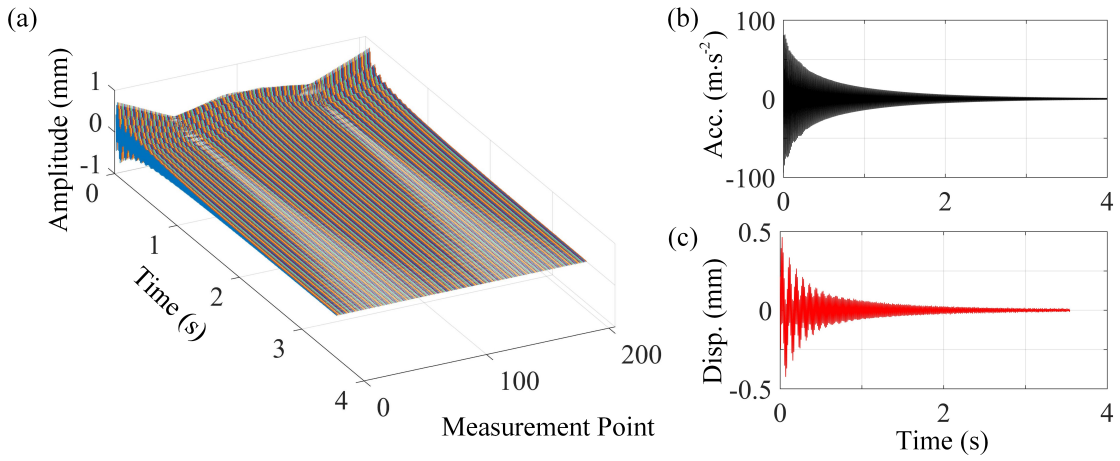

Figure 17: The recorded responses of the beam from DIC and accelerometer, shown are (a) all the recorded responses from DIC, (b) the acceleration time history from the accelerometer, (c) the recorded displacement response at the location with the accelerometer.

amplitude by the PFF method (details can be found in [58] and part II of this paper [1]). The amplitude for acceleration is transferred to amplitude in displacement by dividing by the square of the frequency. The extracted amplitude-time curves and amplitude-time-damping curves from these two data acquisition methods are compared in Fig. 18.

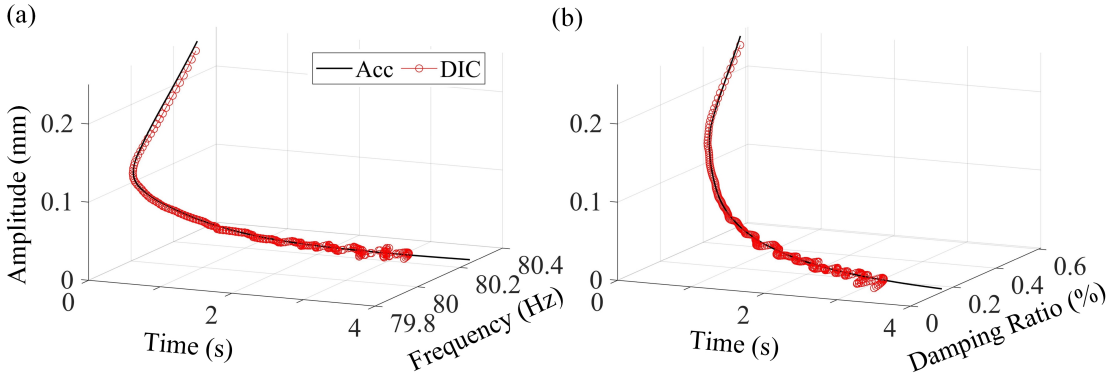

Figure 18: The comparison of the DIC results and the results from the accelerometer, shown are (a) instantaneous frequency and (b) instantaneous damping ratio.

From Fig. 18, it is observed that the amplitude-time-frequency curves and amplitude-time-damping curves are comparable for these two measurement techniques. Therefore, it can be concluded that DIC can be used for further data processing, and as it gives dense measurement data, it is beneficial in obtaining the spatial distribution of nonlinear properties. At low amplitudes (lower than 0.04 mm), the fluctuation from DIC results can be seen because of the video noise in low displacement, but it still shows the same trend with acceleration results.

4.3. Quantification of the Structure's Nonlinearities

A fundamental question in the analysis of nonlinear structures (specifically bolted assemblies) is whether the structure is strongly nonlinear or weakly nonlinear. Weakly nonlinear structures are

amenable to certain modeling assumptions that make numerical analysis more efficient [60]. Central among the assumptions made are that the mode shapes do not change during excitation and that there is no appreciable modal coupling. By contrast, models of strongly nonlinear structures make no such assumptions and often exhibit amplitude evolving mode shapes [61] as well as coupling between modes [62]. As a result, these modeling approaches can be more computationally intensive as higher fidelity models of the joint are necessitated.

4.3.1. Mode Shape Evolution

The evolution of the mode shapes as a function of response amplitude is investigated by using the DIC-based full-field measurement data from fixed sine tests in which the system is driven at resonance. First, the amplitude-control stepped-sine testing (in Section 2.7.1) is conducted to find the natural frequency at the target amplitude level, which shows a 90° phase shift between the excitation force and the acceleration response. Next, the fixed sine testing is conducted at the resonance frequency and response level, and the high-speed cameras are triggered to capture the steady-state vibration of the beam.

The first mode is excited, and the response levels are set as 0.5, 2, 4, 8, and 10 g for accelerometer 3 in Fig. 10. The extracted deflection shape at the highest response amplitude level is shown in Fig. 19 (a). Since the phase shift between the excitation force and the acceleration response is 90°, the deflection shape is the mode shape at the response level. With the increase of the response level from 0.5 to 10 g, the displacement at the left edge of the deflection shape, U_{tip}, increases from approximately 0.03 mm to 0.53 mm. The discontinuous slope can be seen at the edge of the interface (i.e., just to the left of the dashed line indicating the displacement of the middle of the beam, U_{mid}), which is caused by the opening and closing of the joint during the vibration. The discontinuous slope would have appeared on the other side of the interface if the opposite side of the beam were measured. In order to evaluate the variation of the mode shape, the deflection ratios between two locations (U_{tip} and U_{mid} in Fig. 19 (a)) at different response levels are shown in Fig. 19 (b). Due to the low SNR for the 0.5 g response level, the ratio for 0.5 g in Fig. 19 (b) is not in line with the other results. The ratio generally shows an increasing trend from -0.973 to -0.914 with a change of the mode shape of 6%.

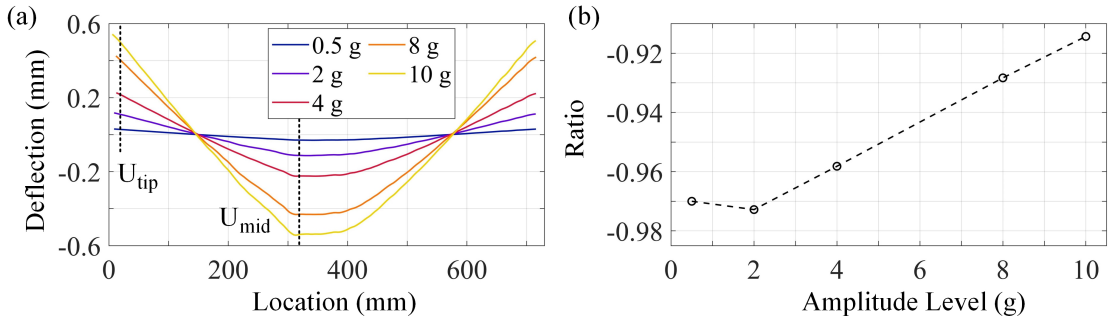

Figure 19: The deflection of the beam and its variation at different response levels, (a) the deflection of the beam at the fixed sine excitation of different levels, (b) the variation of the ratio between the tip and the middle of the beam.

4.3.2. Modal Interactions

The modes for linear structures are independent (one mode will not affect others, and there is no energy transfer between them). However, for nonlinear systems, some modes are coupled, and energy transfer is observed from one mode to another under specific conditions (such as the natural frequencies at a given amplitude being integer multiples of each other). To study the modal interaction in jointed structures, responses under steady-state sinusoidal excitation are used, where the experiment combines the fixed sine testing, amplitude-control stepped sine testing (in Section 2.7.1), and DIC technique.

The test setup is shown in Fig. 10. Three accelerometers are attached to the beam, 1" from the left end, 7" and 3" from the right end. The bolt torque level is kept as 23.7 N·m. The fixed sine and amplitude-control stepped-sine excitations are used to provide steady-state responses. The excitation location is 3" from the right end, which is the node point of mode 3 and is close to the node point of mode 2. Therefore, mode 1 can be sufficiently excited, and modes 2 and 3 are depressed in this excitation condition.

To better understand the vibration behavior, the time history of the accelerometer located at 1" from the left end is shown in a short time window in Fig. 20 (a). Since this accelerometer is not close to the node point of any of the first 3 modes, it should show the resulting response of the first three modes. For the results of Fig. 20 specifically, the excitation frequency is 84 Hz, which is the first modal frequency of the beam, and the excitation level is 10 g. Even though the input signal is sinusoidal, the response contains two main frequency components that are composed of the excitation frequency and the natural frequency of mode 3 (approximately 588 Hz). In Fig. 20 (b), the responses are shown after filtering with a 4th order Butterworth bandpass filter with a middle frequency of 84 Hz (curve 1) and 588 Hz (curve 2). Curve 3 indicates the difference between the raw response and the responses of curve 1 and curve 2 added together. The double reverse filter [58] is used here to guarantee no phase shift for the filtered responses. Even though energy is only put into mode 1 (due to both the excitation frequency and excitation location), a considerable amount of energy flows into mode 3.

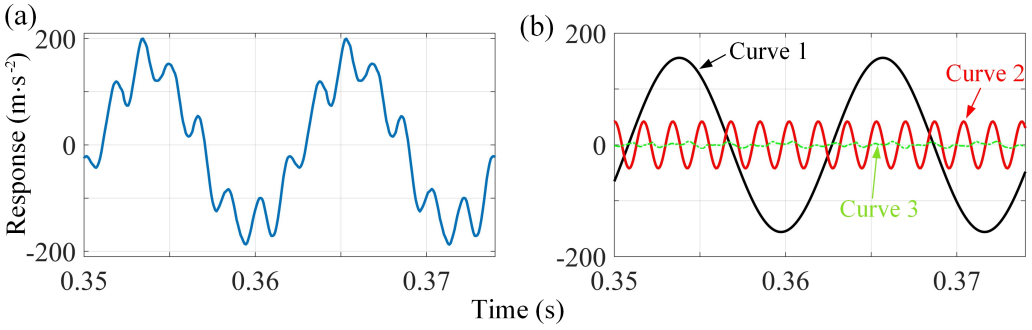

Figure 20: The test setup and the recorded signal from the blue accelerometer, shown are (a) the measured raw response from accelerometer 1 (1 inch from the left end), (b) the decomposed responses.

The modal coupling observed in Fig. 20 is further explored via the DIC measurements. Along the length of the beam, 205 measurement points are recorded with the high speed cameras during steady state excitation. From these measurements, the filtered responses at 84 and 588 Hz are shown in Fig. 21. The resulting shapes are the same as for the first and third mode shapes, providing clear evidence that even though energy is being put into only mode 1, the nonlinear

nature of the system has transferred energy to mode 3.

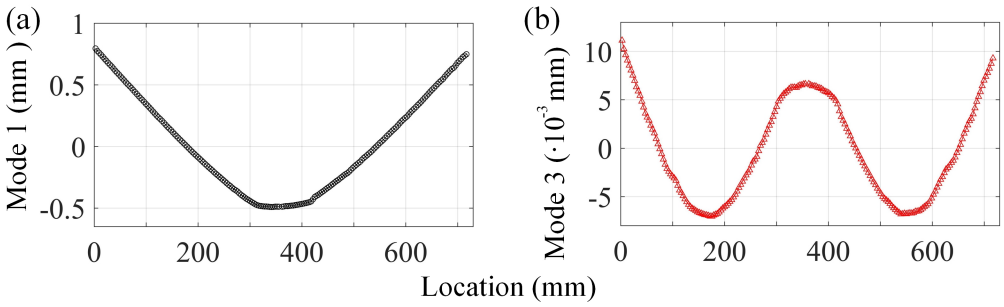

Figure 21: The extracted mode shapes from DIC data, shown are (a) the displacement distribution of component of 84 Hz, (b) the displacement distribution of component of 588 Hz.

To further explore the interaction of the modal coupling and excitation amplitude, an amplitude-control stepped sine test is executed with response amplitudes of 0.5, 1, 2, 4, 6, 10, and 12 g. Here, the response amplitude refers to the steady response amplitude of accelerometer 3 (at the location of the excitation) in Fig. 10. The excitation frequency is from 83 to 85 Hz (in the vicinity of the frequency of mode 1) with a step of 0.05 Hz. For each step, the excitation duration is set as 3 s to reach a steady state.

The variation of the response levels of the mode 1 and mode 3 components measured by the tip accelerometer with respect to the controlled level of mode 1 is shown in Fig. 22 (a) and (b), respectively. Since the response level of mode 1 is controlled during the stepped-sine testing, the response curves in Fig. 22 (a) are approximately constant amplitudes. By contrast, in Fig. 22 (b), each response curve shows a peak for the mode 3 amplitude near an excitation frequency of 84 Hz during the stepped-sine testing. The frequency of the peak shows a small range of variation across the different response levels, which is highlighted by a black dashed line in Fig. 22 (b).

The highest amplitudes of mode 1 and the peak values of the amplitude of mode 3 with different control levels are extracted from Fig. 22 (a) and (b). The peak values are further normalized by dividing the corresponding control level, and the results are shown in Fig. 22 (c). For mode 1, the amplitude ratios are approximately constant (around 2) with the increase of the controlled response level. By contrast, the amplitude ratio curve of mode 3 shows a different trend. The response level of mode 3 is lower than 10% of the input level for low response levels (0 to 4 g). Increasing the input level above 4 g, however, significantly changes the behavior as the response level jumps to 50% of the input level and remains at this percentage as the input is increased further. Thus, there is both a frequency and an amplitude dependence to the existence of modal coupling in this system.

The precise conditions for modal coupling are elucidated through a series of amplitude-controlled stepped-sine tests in which the bolt torques are varied (10 N·m and 19.6 N·m, in addition to the above-described results for 23.7 N·m). It is observed that modal interactions only happen for a bolt torque level of 23.7 N·m , as shown in Table 4. In accordance with the nonlinear dynamics conditions for modal coupling, this is explained by the 23.7 N·m case being the only one in which the third natural frequency is an integer multiple of the first natural frequency. For all other bolt torques investigated, this condition is not met, as shown in Table 4. In other words, as this system is nonlinear, some energy is dissipated through the super-harmonics of the mode being

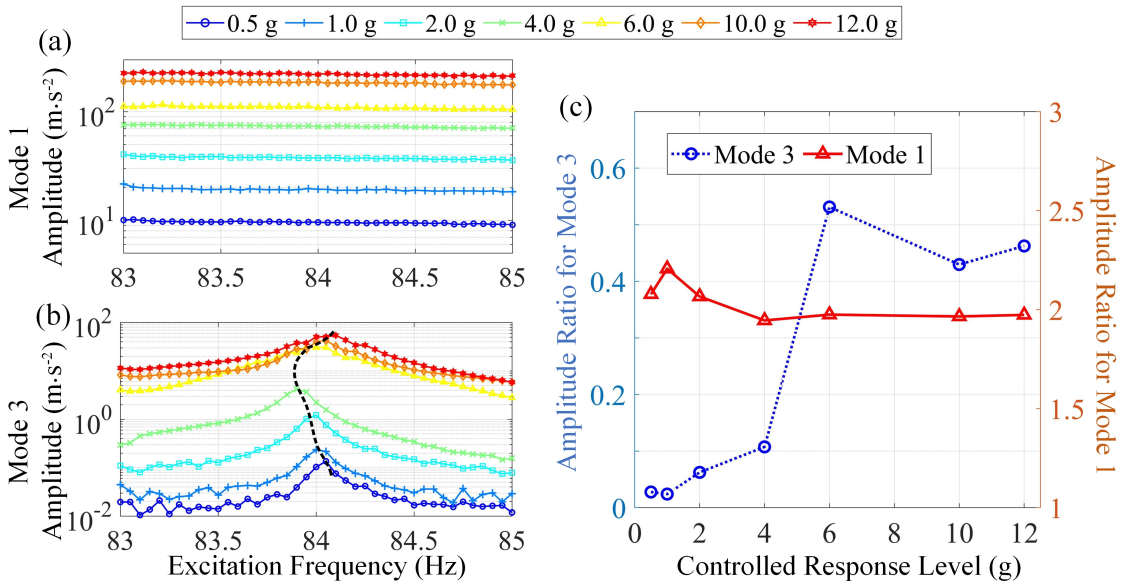

Figure 22: Response levels of mode 1 and mode 3 during the amplitude-controlled stepped-sine testing with different response levels, shown are (a) the amplitude of mode 1 at each step, (b) the amplitude of mode 3 at each step, and (c) the normalized peak values of mode 1 and mode 3 for different controlled levels.

excited. This dissipation is amplified when one of the super-harmonic frequencies is exactly equal to another modal frequency [18, 63].

Table 4: Modal interaction for different bolt torque levels.

Torque (N·m)	f_1 (Hz)	f_2 (Hz)	f_3 (Hz)	f_2/f_1	f_3/f_1	Modal Interaction
23.7 N·m	83.77-84.28	299.81-300.23	589.14-590.16	3.56-3.58	**6.99-7.05**	**Yes**
19.6 N·m	82.97-83.70	299.25-299.96	588.08-589.42	3.56-3.62	7.03-7.10	No
10.2 N·m	79.80-80.03	290.05-290.51	580.21-580.90	3.61-3.66	7.22-7.28	No

5. Conclusions

In this paper, a series of tests are conducted to characterize the dynamic behavior of an assembly that is joined together by a three-bolt lap joint, termed the HBRB. First, the system is characterized using conventional approaches based on accelerometer data. This initial characterization served the dual purpose of both providing a baseline model of the nonlinearity and identifying specific regions that would benefit from additional and more expensive, video-based measurements. DIC was subsequently used to measure a dense, spatio-temporal profile of the displacement of the system during dynamic excitation for multiple types of tests: hammer impact, shaker ringdown, force-control stepped sine sweeps, and amplitude-control stepped sine sweeps. The DIC measurements are extensively validated both from assessments of the noise floor in static tests and through direct comparison with the results of the analysis based on accelerometer data. The DIC data is then used to assess the nonlinear behavior of the system, specifically how the

mode shapes evolve with response amplitude and the conditions necessary for modal coupling to occur. Specific conclusions from this study include:

• DIC is capable of capturing the full-field response of HBRB with sufficient accuracy. In this approach, each camera captures the motion of a half beam to increase the spatial measurement density, and then the spatial data from two cameras are stitched together to obtain the responses of the whole beam. For the current experimental setup, the measurement noise of DIC responses, which comes from the measurement system (including measurement environment, the camera, and DIC method), is about 0.0137 pixels, corresponding to 3.9 μm.

• A novel shaker ringdown testing setup is introduced in this paper. After the shaker excites a particular mode of the HBRB to steady-state, the stinger is detached from the beam, and the free responses of this mode are recorded. With a suitable excitation location, the target mode can be excited to a higher level than hammer testing, which can provide a wider range for amplitude-dependent natural frequency and damping ratio curves.

• Both force-controlled and amplitude-controlled stepped sine tests are used. The amplitude-control tests proved to be a more accurate method to obtain the frequency response functions.

• The identified amplitude-dependent natural frequency and damping ratio curves are comparable for accelerometer and DIC data. The size of the field-of-view for the camera has a great effect on the measurement accuracy of the DIC technique. For the same free response testing, DIC results show consistency with that from accelerometer data, but the accuracy may be lower than acceleration data due to the large field of view (0.36 m in length for 1280 pixels).

• The mode shapes can be extracted from DIC data. With dense spatial data from DIC, the mode shapes of the beam is extracted from the fixed sine testing where the phase difference between the response and the force is 90° at the set response level. Specifically, the ratio of two points on mode 1 shows a 6% variation as the response levels increase from 0.5 g to 10 g.

• A modal interaction is observed for the HBRB when the third natural frequency is an integer multiple of the first natural frequency (in this case, a factor of 7). During the forced response testing, the beam is excited at the node point of mode 3 by the frequency of the first mode. However, there is a significant component of mode 3 in the responses. From the DIC data, the deflection shapes corresponding to the excitation frequency and 7 times of the excitation frequency are extracted, which show similarity with the mode shapes of modes 1 and 3. Additionally, through amplitude-controlled stepped sine testing, the modal interaction behavior is affected by the excitation frequency and response level, which becomes evident for high response levels (more than 4 g for mode 1).

Acknowledgements

This work presents the results of the Tribomechadynamics Research Camp (2019) at Rice University, Houston, Texas, USA (`http://tmd.rice.edu`). The authors appreciate the chance to work together. The authors are also grateful to the SIEMENS and South Central Imaging for their sponsorship. Wei Chen and Mengshi Jin thank China Scholarship Council (CSC) for their financial support at Rice University. Giancarlo Kosova has been supported by the European Union's Horizon 2020 research and innovation program under the Marie Skłodowska-Curie grant agreement No 764547. Debasish Jana and Satish Nagarajaiah acknowledge the grant from the Science and Engineering Research Board of India (SERB).

Data Access

The data used in the paper is available at `https://github.com/mattiacenedese/BRBtesting`.

References

[1] M. Jin, G. Kosova, M. Cenedese, W. Chen, A. Singh, D. Jana, M. R. W. Brake, C. W. Schwingshackl, S. Nagarajaiah, K. Moore, and J. P. Noël. Measurement and identification of the nonlinear dynamics of a jointed structure using full-field data; Part II - Nonlinear System Identification. *Under Review*, 2021.

[2] M. R. W. Brake. *The Mechanics of Jointed Structures: Recent Research and Open Challenges for Developing Predictive Models for Structural Dynamics*. Springer, 2017.

[3] L. Gaul and R. Nitsche. The role of friction in mechanical joints. *Applied Mechanics Reviews*, 54(2):5173–84, 2001.

[4] C. W. Schwingshackl, D. Di Maio, I. Sever, and J. S. Green. Modeling and validation of the nonlinear dynamic behavior of bolted flange joints. *Journal of Engineering for Gas Turbines and Power*, 135(12):122504, 2013.

[5] G. Kerschen, K. Worden, A. F. Vakakis, and J. C. Golinval. Past, present and future of nonlinear system identification in structural dynamics. *Mechanical Systems and Signal Processing*, 20(3):505–592, 2006.

[6] J. P. Noel and G. Kerschen. Nonlinear system identification in structural dynamics: 10 more years of progress. *Mechanical Systems and Signal Processing*, 83:2–35, 2017.

[7] SL. Brunton, JL. Proctor, and JN. Kutz. Discovering governing equations from data by sparse identification of nonlinear dynamical systems. *Proceedings of the national academy of sciences*, 113(15):3932–3937, 2016.

[8] Z. Lai and S. Nagarajaiah. Sparse structural system identification method for nonlinear dynamic systems with hysteresis/inelastic behavior. *Mechanical Systems and Signal Processing*, 117:813–842, 2019.

[9] K Worden, RJ Barthorpe, EJ Cross, N Dervilis, GR Holmes, G Manson, and TJ Rogers. On evolutionary system identification with applications to nonlinear benchmarks. *Mechanical Systems and Signal Processing*, 112:194–232, 2018.

[10] M. Jin, M. R. W. Brake, and H. Song. Comparison of nonlinear system identification methods for free decay measurements with application to jointed structures. *Journal of Sound and Vibration*, 453:268–293, 2019.

[11] P. A. Atkins, J. R. Wright, and K. Worden. An extension of force appropriation to the identification of non-linear multi-degree of freedom systems. *Journal of Sound and Vibration*, 237(1):23–43, 2000.

[12] M. Peeters, G. Kerschen, and J. Golinval. Modal testing of nonlinear vibrating structures based on nonlinear normal modes: experimental demonstration. *Mechanical Systems and Signal Processing*, 25(4):1227–1247, 2011.

[13] C. W. Schwingshackl, C. Joannin, L. Pesaresi, J. S. Green, and N. Hoffmann. *Test method development for nonlinear damping extraction of dovetail joints*, pages 229–237. Springer, 2014.

[14] S. Catalfamo, S. A. Smith, F. Morlock, M. R. W. Brake, P. Reuß, C. W. Schwingshackl, and W. Zhu. *Effects of experimental methods on the measurements of a nonlinear structure*, pages 491–500. Springer, 2016.

[15] G. Gloth and M. Sinapius. Influence and characterisation of weak non-linearities in swept-sine modal testing. *Aerospace Science and Technology*, 8(2):111–120, 2004.

[16] J. R. Wright, J. E. Cooper, and M. J. Desforges. Normal-mode force appropriation—theory and application. *Mechanical Systems and Signal Processing*, 13(2):217–240, 1999.

[17] J. Lau, B. Peeters, J. Debille, Q. Guzek, and T. Kahlmann. *Ground Vibration Testing Master Class: modern testing and analysis concepts applied to an F-16 aircraft*, volume 1 of *Advanced Aerospace Applications*. Springer New York, 2011.

[18] G. Kerschen, M. Peeters, J. Golinval, and A. F. Vakakis. Nonlinear normal modes, part i: A useful framework for the structural dynamicist. *Mechanical Systems and Signal Processing*, 23(1):170–194, 2009.

[19] L. Renson, A. Gonzalez-Buelga, D. A. W. Barton, and S. A. Neild. Robust identification of backbone curves using control-based continuation. *Journal of Sound and Vibration*, 367:145–158, 2016.

[20] S. Peter, R. Riethmüller, and R. I. Leine. *Tracking of Backbone Curves of Nonlinear Systems Using Phase-Locked-Loops*. Springer International Publishing, 2016.

[21] M. Scheel, S. Peter, R. I. Leine, and M. Krack. A phase resonance approach for modal testing of structures with nonlinear dissipation. *Journal of Sound and Vibration*, 435:56–73, 2018.

[22] J. P. Noël and G. Kerschen. Frequency-domain subspace identification for nonlinear mechanical systems. *Mechanical Systems and Signal Processing*, 40(2):701–717, 2013.

[23] S. L. Lacy and D. S. Bernstein. Subspace identification for non-linear systems with measured-input non-linearities. *International Journal of Control*, 78(12):906–926, 2005.

[24] S. Marchesiello and L. Garibaldi. A time domain approach for identifying nonlinear vibrating structures by subspace methods. *Mechanical Systems and Signal Processing*, 22(1):81–101, 2008.

[25] J. P. Noel, A. F. Esfahani, G. Kerschen, and J. Schoukens. A nonlinear state-space approach to hysteresis identification. *Mechanical Systems and Signal Processing*, 84:171–184, 2017.

[26] C. Warren, C. Niezrecki, P. Avitabile, and P. Pingle. Comparison of frf measurements and mode shapes determined using optically image based, laser, and accelerometer measurements. *Mechanical Systems and Signal Processing*, 25(6):2191–2202, 2011.

[27] P. L. Reu, D. P. Rohe, and L. D. Jacobs. Comparison of DIC and LDV for practical vibration and modal measurements. *Mechanical Systems and Signal Processing*, 86:2–16, 2017.

[28] W. Chen, X. Zang, S. Wu, M. Jin, and H. Song. Gradient-based point tracking method and its application in the modal test of a solar array model. *Measurement*, 2020.

[29] S. Bhowmick, S. Nagarajaiah, and Z. Lai. Measurement of full-field displacement time history of a vibrating continuous edge from video. *Mechanical Systems and Signal Processing*, 144:106847, 2020.

[30] S. Bhowmick and S. Nagarajaiah. Identification of full-field dynamic modes using continuous displacement response estimated from vibrating edge video. *Journal of Sound and Vibration*, 489:115657, 2020.

[31] Wei Chen, Mengshi Jin, Jiasheng Huang, Yuanchang Chen, and Hanwen Song. A method to distinguish harmonic frequencies and remove the harmonic effect in operational modal analysis of rotating structures. *Mechanical Systems and Signal Processing*, 2021.

[32] TC Chu, WF Ranson, and Michael A Sutton. Applications of digital-image-correlation techniques to experimental mechanics. *Experimental mechanics*, 25(3):232–244, 1985.

[33] Bing Pan, Kemao Qian, Huimin Xie, and Anand Asundi. Two-dimensional digital image correlation for in-plane displacement and strain measurement: a review. *Measurement science and technology*, 20(6):062001, 2009.

[34] Michael A Sutton, Jean Jose Orteu, and Hubert Schreier. *Image correlation for shape, motion and deformation measurements: basic concepts, theory and applications*. Springer Science & Business Media, 2009.

[35] Javad Baqersad, Peyman Poozesh, Christopher Niezrecki, and Peter Avitabile. Photogrammetry and optical methods in structural dynamics–a review. *Mechanical Systems and Signal Processing*, 86:17–34, 2017.

[36] D. M. Feng and M. Q. Feng. Experimental validation of cost-effective vision-based structural health monitoring. *Mechanical Systems and Signal Processing*, 88:199–211, 2017.

[37] Billie F Spencer Jr, Vedhus Hoskere, and Yasutaka Narazaki. Advances in computer vision-based civil infrastructure inspection and monitoring. *Engineering*, 5(2):199–222, 2019.

[38] T. J. Beberniss and D. A. Ehrhardt. High-speed 3D digital image correlation vibration measurement: Recent advancements and noted limitations. *Mechanical Systems and Signal Processing*, 86:35–48, 2017.

[39] Debasish Jana and Satish Nagarajaiah. Computer vision-based real-time cable tension estimation in Dubrovnik cable-stayed bridge using moving handheld video camera. *Structural Control and Health Monitoring*, 28(5):e2713, 2021.

[40] B. Pan, K. Qian, H. Xie, and A. Asundi. Two-dimensional digital image correlation for in-plane displacement and strain measurement: a review. *Measurement science and technology*, 20(6):062001, 2009.

[41] D. A. Ehrhardt, M. S. Allen, S. F. Yang, and T. J. Beberniss. Full-field linear and non-linear measurements using continuous-scan laser doppler vibrometry and high speed three-dimensional digital image correlation. *Mechanical Systems and Signal Processing*, 86:82–97, 2017.

[42] T. Bregar, K. Zaletelj, G. Cepon, J. Slavic, and M. Boltezar. Full-field FRF estimation from noisy high-speed-camera data using a dynamic substructuring approach. *Mechanical Systems and Signal Processing*, 150:12, 2021.

[43] A. Singh and K. J. Moore. Characteristic nonlinear system identification of local attachments with clearance nonlinearities. *Nonlinear Dynamics*, 102(3):1667–1684, 2020.

[44] W. Chen, M. Jin, I. Lawal, M. R. W. Brake, and H. Song. Measurement of slip and separation in jointed structures with non-flat interfaces. *Mechanical Systems and Signal Processing*, 134:22, 2019.

[45] M. Brøns, T. A. Kasper, G. Chauda, S. W. B. Klaassen, C. W. Schwingshackl, and M. R. W. Brake. Experimental Investigation of Local Dynamics in a Bolted Lap Joint Using Digital Image Correlation. *Journal of Vibration and Acoustics*, 142(5), 07 2020.

[46] P. Poozesh, J. Baqersad, C. Niezrecki, P. Avitabile, E. Harvey, and R. Yarala. Large-area photogrammetry based testing of wind turbine blades. *Mechanical Systems and Signal Processing*, 86:98–115, 2017.

[47] M. R. W. Brake, C. W. Schwingshackl, and P. Reuss. Observations of variability and repeatability in jointed structures. *Mechanical Systems and Signal Processing*, 129:282–307, 2019.

[48] T. Dossogne, T. W. Jerome, D. P. T. Lancereau, S. A. Smith, M. R. W. Brake, B. R. Pacini, P. Reuss, and C. W. Schwingshackl. *Experimental assessment of the influence of interface geometries on structural dynamic response*, pages 255–261. Springer, 2017.

[49] A. Fantetti, L. R. Tamatam, M. Volvert, I. Lawal, L. Liu, L. Salles, M. R. W. Brake, C. W. Schwingshackl, and D. Nowell. The impact of fretting wear on structural dynamics: Experiment and simulation. *Tribology International*, 138:111–124, 2019.

[50] Z. Zhang. A flexible new technique for camera calibration. *IEEE Transactions on Pattern Analysis and Machine Intelligence*, 22:1330–1334, 2000.

[51] S. Urban, J. Leitloff, and S. Hinz. Improved wide-angle, fisheye and omnidirectional camera calibration. *ISPRS Journal of Photogrammetry and Remote Sensing*, 108:72–79, 2015.

[52] P. Reu. All about speckles: Speckle size measurement. *Experimental Techniques*, 38(6):1–2, 2014.

[53] D. Z. Turner. Digital image correlation engine (DICe) reference manual. *Sandia Nat. Lab., Livermore, CA, USA, Sandia Rep. SAND2015-10606 O*, 2015.

[54] T Mace, J Taylor, and CW Schwingshackl. A novel technique to extract the modal damping properties of a thin blade. In *Topics in Modal Analysis & Testing, Volume 8*, pages 247–250. Springer, 2020.

[55] D. Jana, S. Mukhopadhyay, and S. Ray-Chaudhuri. Fisher information-based optimal input locations for modal identification. *Journal of Sound and Vibration*, 459:114833, 2019.

[56] W. Chen, M. S. Jin, and H. W. Song. Optimal configuration of shakers for phase resonance testing using modal parameters. *Proceedings of the Institution of Mechanical Engineers Part C-Journal of Mechanical Engineering Science*, 233(16):5676–5690, 2019.

[57] H. Goyder. Signal processing methods for determining the properties of bolted joints. In *ASME 2015 International Design Engineering Technical Conferences and Computers and Information in Engineering Conference*, pages V008T13A024–V008T13A024. American Society of Mechanical Engineers, 2015.

[58] M. Jin, W. Chen, M. R. W. Brake, and H. Song. Identification of instantaneous frequency and damping from transient decay data. *Journal of Vibration and Acoustics*, 142(5), 2020.

[59] S. A. Smith, M. R. W. Brake, and C. W. Schwingshackl. On the characterization of nonlinearities in assembled structures. *Journal of Vibration and Acoustics*, 142(5):11, 2020.

[60] D. R. Roettgen and M. S. Allen. Nonlinear characterization of a bolted, industrial structure using a modal framework. *Mechanical Systems and Signal Processing*, 84:152–170, 2017.

[61] N. N. Balaji, W. Chen, and M. R. W. Brake. Traction-based multi-scale nonlinear dynamic modeling of bolted joints: Formulation, application, and trends in micro-scale interface evolution. *Mechanical Systems and Signal Processing*, 139:32, 2020.

[62] M. Krack. Nonlinear modal analysis of nonconservative systems: Extension of the periodic motion concept. *Computers and Structures*, 154:59–71, 2015.

[63] K. J. Moore, M. Kurt, M. Eriten, D. M. McFarland, L. A. Bergman, and A. F. Vakakis. Direct detection of nonlinear modal interactions from time series measurements. *Mechanical Systems and Signal Processing*, 2017.